Applied Catalysis B: Environment and Energy 344 (2024) 123671

Contents lists available at ScienceDirect

Applied Catalysis B: Environment and Energy

journal homepage: www.elsevier.com/locate/apcatb

Nickel aluminate spinel-derived catalysts for aqueous-phase hydrogenolysis of glycerol with in-situ hydrogen production: Effect of molybdenum doping

D. Gallego-García [a], U. Iriarte-Velasco [b], M.A. Gutiérrez-Ortiz [a], J.L. Ayastuy [a,*]

[a] Department of Chemical Engineering, Faculty of Science and Technology, University of the Basque Country UPV/EHU, Sarriena S/N, 48940 Leioa, Spain
[b] Department of Chemical Engineering, Faculty of Pharmacy, University of the Basque Country UPV/EHU, Paseo de la Universidad, 701006 Vitoria, Spain

ARTICLE INFO

Keywords:
Glycerol
Hydrogenolysis
Nickel aluminate spinel
Molybdenum
1,2-Propylene glycol

ABSTRACT

The correlation between the physico-chemical properties of bare and Mo-doped nickel aluminate derived catalysts and product distribution during hydrogenolysis of glycerol with in situ produced hydrogen in continuous was investigated. Stoichiometric nickel aluminate spinel was synthesized via citrate sol-gel in a one-pot synthesis and subsequently doped it with 1 wt% Mo, using both sol-gel one-pot and impregnation methods. Catalytic runs were performed at 235 ºC/ 45 bar for 4 h TOS. The results indicate that Mo-doping increased the number of both metal and acid sites, leading to more selectivity towards deoxygenated products. 1,2-propylene glycol was the major liquid product, Mo/NiAl catalyst exhibited the highest yield (27%) and selectivity (39%). Post-reaction characterization revealed that leaching and oxidation of metals could potentially cause catalyst deactivation. 1 wt% Mo-doped nickel aluminate-derived catalysts possess potential for the selective production of 1,2-PG in a eco-friendly process through one-pot coupling H_2 generation and hydrogenolysis reactions.

1. Introduction

The global dependence on fossil fuels and the consequential significant generation of greenhouse gases (GHGs) have compelled scientific action to mitigate the effects of climate change [1]. The utilization of biomass to produce high-value chemicals presents the possibility of substituting fossil fuel-dependent processes. Glycerol, the primary by-product of the biodiesel production, is one of the 12 platform molecules for biorefineries identified by the DOE. Since refining crude glycerol to a higher grade is a costly process that is not viable for small and medium-sized plants, valorization by producing energy and value-added chemicals is an economically promising alternative [2]. The highly functionalized glycerol molecule, in comparison to hydrocarbons, has the potential to produce a wide range of value-added chemicals through numerous chemical reactions [3]. Among them, dehydration, hydrogenolysis, and aqueous phase reforming (APR) reactions are particularly significant [4].

To enable the conversion of glycerol into high value-added chemicals, the oxygen content must be decreased [5]. The removal of excess oxygen can be achieved through a hydrogenolysis (also called hydrodeoxygenation, HDO), which involves C-O bond cleavage and subsequent addition of hydrogen [6]. Selective hydrogenolysis of C-O bonds by hydrogen, is considered an atom-economical and cost-competitive process. By glycerol hydrogenolysis high value-added chemicals such as 1,2-propylene glycol and 1,3-propylene glycol can be obtained [7].

Conventionally, the hydrogen required for the hydrogenolysis of glycerol has been externally supplied at high pressure [8]. Safety issues, the use of fossil resources for its production and the low solubility of gas hydrogen in water [9] are the main drawbacks for its implementation at large scale. A promising and of great interest alternative consists in the in situ production of hydrogen. This can be done via Catalytic Transfer Hydrogenation (CTH) reaction where hydrogen is formed from a hydrogen donor [10], added externally. More advantageous is to couple to the aqueous phase reforming (APR) of glycerol, since it does not necessitate the addition of any hydrogen donor. The APR of glycerol is a one-step catalytic process that operates in the liquid phase at low temperature (200–250 ºC) and pressure enough to maintain reactants in a liquid state [11]. As a result, there is no need to evaporate the feedstream. By selecting the appropriate catalysts and reaction conditions, the reaction can selectively produce H_2 while sacrificing only a fraction of the substrate [2,12]. Given that the APR and hydrogenolysis are carried out under comparable operational conditions [13], their integration in a one-pot reaction is straightforward.

In this one-pot system, in situ H_2 is produced by APR, which consists

* Corresponding author.
E-mail address: joseluis.ayastuy@ehu.eus (J.L. Ayastuy).

https://doi.org/10.1016/j.apcatb.2023.123671
Received 6 November 2023; Received in revised form 21 December 2023; Accepted 27 December 2023
Available online 29 December 2023
0926-3373/© 2023 The Author(s). Published by Elsevier B.V. This is an open access article under the CC BY license (http://creativecommons.org/licenses/by/4.0/).

of preferential C-H and C-C bond cleavages to produce H_2 and CO, the latter being converted to CO_2 by Water-Gas Shift (WGS) reaction. The resulting H_2 is then used to cleave the C-O bond of the glycerol dehydration intermediate to produce propylene glycol [14]. A dual-function catalyst is crucial as there are required the presence of both metal and acid sites. The acid function plays a key role in securing the adsorption and activation sites for the oxygen of O-containing compounds (C-O bond cleavage), while the metal sites produce hydrogen (C-H and C-C bonds cleavage) and also activate hydrogen species that will subsequently hydrogenate the activated O-containing compounds. The competing reactions in the hydrogenolysis of glycerol involve the cleavage of a C-C bond, resulting in less valuable degradation products [10]. Thus, a well-balanced ratio of acidic and metallic sites is crucial.

Recent reviews have summarized relevant catalytic systems for the glycerol hydrogenolysis reaction [15,16]. Many works have been published on glycerol hydrogenolysis, the vast majority using external hydrogen. Catalysts containing noble metals such as Pt [17,18] or Ru [19,20] supported on different acid supports, including ZrO_2, SiO_2-Al_2O_3, HZSM-5, WOx-ZrO_2 and Nb_2O_5, are commonly utilized. However, their tendency to catalyze the cleavage of C-C bonds renders them less selective than transition metals towards propylene glycols. The incorporation of oxophilic elements such as Mo or W to promote the acidity [18,21] and the C-O bond scission [22] have been reported to increase the selectivity to propylene glycols. As an alternative to noble metals, transition metal catalysts have been also investigated for glycerol HDO, being Cu, Co and Ni the most frequently utilized [3].

Currently, only a few studies have been reported on hydrogenolysis of glycerol with in situ-formed hydrogen. Among the studied catalysts, Ni is the most employed metal due to its high APR and hydrogenolysis ability [23], but also noble metals [24], Cu [25] or bimetallic [13,26,27] are being investigated. In our previous work [23] we successively produced H_2 by glycerol APR using Ni-based catalysts derived from nickel aluminate spinel, since small nickel particles with high intrinsic activity were formed upon high temperature reduction. Therefore, in order to optimize the catalyst for propylene glycol production and improve the selectivity to C-O cleavage products, enhancing its acidity is necessary.

With this background, here we study the impact of molybdenum doping on the physico-chemical and catalytic characteristics of nickel-based catalysts. To the best of our knowledge, the effects of molybdenum doping on the properties and catalytic performance of nickel aluminates used in the hydrogenolysis of glycerol with in situ-generated hydrogen have not yet investigated. Two different techniques of Mo doping were used to create bulk-doped (via sol-gel) and surface-doped (via impregnation) catalysts with a Mo content of 1 wt%. The obtained catalysts were systematically characterized in both calcined and reduced state in order to establish structure-activity correlation. Additionally, spent catalysts were characterized to identify the primary deactivation causes.

2. Experimental

2.1. Catalysts synthesis

Stoichiometric nickel aluminate (NiAl) was synthesized as a reference catalyst using the sol-gel method in a one-pot synthesis. Firstly, a suitable amount of nickel (II) nitrate hexahydrate (Alfa Aesar) and aluminium nitrate nonahydrate (Supelco) were dissolved in deionized water separately at room temperature before being mixed together. Additionally, an aqueous solution of the chelating agent citric acid (Sigma Aldrich) was prepared at a molar ratio of citric acid to metals of 1.2:1. The latter solution was dropwise added to metal-containing solution while stirring for an hour under room temperature. The solution was further heated to 70 °C and continuously stirred magnetically to remove excess water, which yielded a green gel. The gel was then dried overnight at 100 °C to produce a foamy solid. Subsequently, the solid was calcined in air at 850 °C in a muffle for 4 h (heating rate of 2 °C/min).

The MoNiAl catalyst was synthesized using a one-pot method, whereby a suitable amount of ammonium molybdate tetrahydrate (Sigma Aldrich) was added to the metal solution to achieve a 1 wt% Mo loading in the final solid.

The Mo/NiAl catalyst was synthesized by wet impregnation of 1 wt% Mo onto the NiAl support, with ammonium molybdate tetrahydrate being employed as the metal precursor. The resultant solid was dried overnight at 100 ºC before being calcined in a muffle for 2 h at 400 ºC (with heating at a rate of 2 ºC/min).

2.2. Catalysts characterization

The bulk chemical composition of the synthesized solids was assessed via X-ray fluorescence (XRF) using the AXIOS equipment. Metal leaching levels during catalytic runs were analyzed through inductively coupled plasma mass spectroscopy (ICP-MS) (XSeries 2).

For textural properties (specific surface area, volume, and pore size distribution) N_2 adsorption-desorption isotherms were utilized at 77 K in Micromeritics TRISTAR II 3020 equipment. The sample underwent outgassing at 300 ºC for 10 h to eliminate any moisture and adsorbed impurities. The BET formalism was utilized to determine the specific surface area, while the BJH method was used to obtain the pore size distribution (PSD) through the desorption branch of the isotherms.

Crystalline phases were identified via X-ray diffraction (XRD) using the PANalytical Xpert PRO diffractometer, equipped with a copper tube (λ = 1.5418 Å). The PANalytical X′pert HighScore software has been utilized with the ICDD database to identify the phases present in the samples. The Scherrer equation was applied to calculate the crystallite size of each species from the line broadening of its most prominent peak. Additionally, the lattice parameter (a) for a cubic crystal structure was calculated using Eq. 1.

$$a = \frac{\lambda}{2\sin\theta}\sqrt{h^2 + k^2 + l^2} \quad (1)$$

were θ is the diffraction angle; and h, k and l are the Miller indices.

The reducibility of the solids was examined through H_2-TPR using hydrogen as the reducing gas in a Micromeritics Autochem 2920 instrument. The calcined sample, around 50 mg, underwent pre-treatment in a He stream at 550 ºC (heating rate of 10 ºC/min, held for 1 h) to eliminate impurities. It was then cooled to 50 ºC in He flow. The sample underwent the passing of 5% H_2/Ar flow simultaneously with an increase in temperature up to 950 ºC (heating rate of 10 ºC/min, held for 30 min). The TPR_{950} profile was monitored using a Thermal Conductivity Detector (TCD), which analyzed the reactor exhaust after water trapping. The TPR_{700} profile was obtained by following the same protocol but heating up to 700 ºC and holding for 2 h. The degree of reduction was calculated as the ratio of hydrogen uptakes TPR_{700}/TPR_{950}.

The active surface area of metallic Ni per catalyst gram (S_{Ni^o}) was determined using the double isotherm method via static H_2 chemisorption on a Micromeritics ASAP 2020 apparatus. A U-shaped quartz tube containing around 0.3 g of ex-situ reduced and passivated catalyst (details of conditions used below) was positioned between two layers of quartz wool. Preparation for the experiment involved the following steps: firstly, degasification at 350 °C under helium was performed in order to remove any adsorbed compounds; secondly, reduction under a flow of hydrogen at 350 °C for one hour was carried out; thirdly, evacuation at 360 °C for one and a half hours was completed; and finally the sample was cooled down to 35 °C under vacuum. Subsequently, two consecutive H_2 adsorption isotherms were collected with an in-between evacuation. The quantity of Ni^0 atoms that were exposed was calculated by considering the volume of chemisorbed H_2, assuming a H/Ni stoichiometry of 1/1. The nickel surface area (S_{Ni^o}) was calculated based on a cross-sectional area of 0.065 nm^2/at_{Ni}. The capability of metallic sites

for H_2 adsorption and activation was analyzed using H_2-TPD on a Micromeritics Autochem 2920 instrument. About 20 mg of the sample was first reduced in a 5% H_2/Ar flow at temperatures up to 700 ºC, with a heating rate of 10 ºC/min. The sample was then held for 1 h, and subsequently cooled to 40 ºC in He flow before being saturated in pure H_2 flow for 1 h. The temperature was then gradually increased up to 700 ºC, with a heating rate of 10 ºC/min, in an Ar flow, and the exhaust gases were monitored by TCD.

The coordination and oxidation states of nickel cations were analyzed using UV–VIS diffuse reflectance spectroscopy. The instrument utilized was a UV–vis–NIR Cary 5000 coupled with an integrating sphere of diffuse reflectance (Varian), operating in a range of 200 to 2500 nm. The reflectance data was converted to absorption via the Kubelka-Munk transformation.

Additionally, the acidity of the solids in their reduced forms was assessed through ammonia pulse chemisorption. The solid (about 0.1 g) underwent a reduction step (by flowing 5% H_2/He at 700 ºC, heating at a rate of 10 ºC/min, and held for 1 h). After cooling to 90 °C, a series of pulses of 10% NH_3/He (with 30 min sweep time with He between pulses) were introduced at 90 ºC until a constant peak area was achieved.

The catalysts were characterized using Raman spectroscopy, as were the carbonaceous deposits in the spent catalysts. The measurements were conducted using a Renishaw InVia Raman spectrometer, which was attached to a Leica DMLM microscope. A 514 nm laser (ion-argon laser, Modu-Laser) was employed while reducing laser power to prevent samples from undergoing photo-decomposition via neutral density filters. To enhance the signal-to-noise ratio, spectra were captured for 40 s with an accumulation of 10 scans at 10% of the maximum 514 nm laser power within the spectral window ranging from 200 cm^{-1} to 2000 cm^{-1}.

X-ray photoelectron spectroscopy (XPS) was utilized to conduct a surface chemical-state analysis of Ni, Al, and Mo. The measurements were done using a SPECS spectrometer with a Phoibos 150 1D-DLD analyzer and a monochromatic Al Kα (1486.7 eV) radiation source. The detailed peaks were deconvoluted after Shirley background subtraction utilizing a mixed Gaussian-Lorentzian function through the use of CASA XPS software. The binding energies (BE) were calibrated with reference to the C 1 s peak (284.6 eV) of adventitious carbon. Concentrations were determined by adjusting the values with relative atomic sensitivity factors (Scofield).

Imaging with scanning transmission electron microscopy (STEM) and EDS were conducted with a probe-corrected FEI Titan 60–300 operating at 300 kV. The instrument was installed with a high brightness X-FEG and a Cs CESCOR corrector for the condenser system, allowing for sub-angstrom probe size. To analyze the chemical composition, elemental maps were generated using an Ultim Max detector (Oxford Instruments) to obtain X-ray Energy Dispersive Spectra (EDS). For STEM observations, ethanolic suspension containing NPs was dropped onto a holey carbon-coated copper micro-grid. SEM-EDS of the spent catalysts was performed in the Carl Zeiss EVO 40 equipment equipped with an Oxford Instrument X-Max EDS detector.

Carbonaceous deposits on spent catalysts were quantified by H_2-TPR coupled to mass spectroscopy (H_2-TPR-MS). The H_2-TPR was performed on Micromeritics Autochem 2920 instrument, and the exhaust was followed by MS (Pffeifer Vacuum OmniStar). First, c.a. 0.05 g of the spent catalyst was cleaned under a He flow, at 400 ºC for 1 h (heating ramp of 10 ºC/min ramp) in order to remove absorbed organics. After cooling to 40 ºC, 5%H_2/Ar flow was passed through the sample while heating at 10 ºC/min up to 950 ºC. The *m/z* signals 15 (CH_4) and 18 (water) were followed. For the quantification, the MS was calibrated for CH_4.

2.3. Catalytic performance

The aqueous-phase glycerol hydrogenolysis was performed in a fixed-bed up-flow reactor (Microactivity Effi, PID Eng&Tech) (Fig. S1, ESI) operating at a temperature of 235 ºC and a pressure of 45 bar, using a feedstream containing 10 wt% glycerol aqueous solution, comparable to the composition derived from the production of biodiesel, after removing alcohol and neutralizing the acidic fraction. A standard run (WHSV=12 h^{-1}) involved placing 0.5 g of a catalyst (0.04–0.16 mm diameter) on a stainless-steel frit and covering it with a quartz wool plug. The catalyst was then reduced in-situ, using a 10% H_2/He flow, at a temperature of 700 ºC and atmospheric pressure over a period of 2 h (heating rate 5 ºC/min). The He pressure was applied to the reactor. Once the desired pressure was reached, the He flow was changed to bypass and the HPLC pump (Eldex optos 5985–1LMP) was activated at a flow rate of 0.1 mL/min. Simultaneously, the reactor temperature was increased gradually (at a rate of 5 ºC/min) until the reaction temperature was attained. The impact of contact time was analyzed based on WHSV (range 6–36 h^{-1}), by modifying the feedstream flowrate over 0.5 g of catalyst. The reaction products were cooled using a Peltier cell and subsequently separated into two distinct phases. The non-condensed gases underwent online analysis using a μGC (Agilent 490) equipped with four columns (Al_2O_3-KCl, PPQ, MS5A with He as the carrier, and MS5A with Ar as the carrier). The liquid products were collected every hour in sealed vials and then analyzed offline by GC-FID (Agilent 6890 N, DB-Heavy Wax column). The gases that were calibrated included C1-C5 alkanes, C2-C3 alkenes, H_2, CO, CO_2 and He as an internal standard. The calibration for the GC-FID analysis comprised 12 products, which included glycerol. Total organic carbon (TOC) in the liquid phase was measured using a Shimadzu TOC-L apparatus and used in the carbon balance calculation. The total conversion of glycerol (X_{Gly}) was calculated as follows:

$$X_{Gly}(\%) = 100 \times \frac{F^{in}_{Glycerol} - F^{out}_{Glycerol}}{F^{in}_{Glycerol}} \tag{2}$$

where $F^{in}_{Glycerol}$ and $F^{out}_{Glycerol}$ represent the molar flow of glycerol at the inlet and outlet of the reactor, respectively. The yields of carbon to liquids (Y_{Liquid}) and to gases (Y_{Gases}) were calculated using the following formulae:

$$Y_{Liquid}(\%) = 100 \times \frac{\sum_i C_i \times F_{L,i}}{3 \times F^{in}_{Glycerol}} \tag{3}$$

$$Y_{Gas}(\%) = 100 \times \frac{\sum_j C_j \times F_{G,j}}{3 \times F^{in}_{Glycerol}} \tag{4}$$

where the molar flow of each liquid compound ($F_{L,i}$) and gas compound ($F_{G,j}$) is multiplied by the number of carbon in each compound (C_i and C_j). The selectivity for the liquid product i (S_i) was calculated using the Eq. (5).

$$S_i(\%) = 100 \times \frac{C_i \times F_{L,i}}{3 \times \left(F^{in}_{Glycerol} - F^{out}_{Glycerol}\right)} \tag{5}$$

The degree of oxygen removal or degree of deoxygenation (DOD), was calculated as follows:

$$DOD(\%) = 100 \times \frac{3 \times F^{in}_{Glycerol} - \sum_i O_i \times F_{L,i}}{3 \times F^{in}_{Glycerol}} \tag{6}$$

where O_i is the molar the number of oxygen in each compound. The reaction rate for 1,2-propylene glycol (1,2-PG) production was given as the site-time yield (STY_{PG}), defined as the number of moles formed per catalytic metal active site per minute, and normalized to metallic surface sites from H_2 chemisorption.

3. Results and discussion

3.1. Chemical composition and textural properties

The bulk chemical composition of all the solids was close to the target for all elements (Table S1, ESI). For the Mo/NiAl solid, the Mo loading corresponded to 0.68 at_{Mo}/nm^2 (about 0.15 monolayer coverage).

The N_2 adsorption-desorption isotherms (Fig. S2(A), ESI) of the calcined solids were of type IV(a) with hysteresis of type H2(b) from the IUPAC classification, characteristics of mesoporous materials. The isotherm remained nearly horizontal over the upper range of relative pressure, indicating little contribution of macropores [28]. For the MoNiAl solid, the flat region of the isotherm was shorter (i.e. desorption branch separation occurred at higher partial pressure), indicating larger pore size. This was confirmed by the upshift of its main peak in the BJH pore size distribution (Fig. S2(B), ESI). It also had a bimodal pore distribution (maxima at 3.4 and 6.0 nm). In contrast, the PSD of the calcined NiAl and Mo/NiAl samples were similar, showing unimodal and narrow distributions. The PSD curves confirmed that a mesoporous material was synthesized. In addition, the pore volume decreased upon Mo doping, consistent with the decrease in S_{BET}.

Upon reduction, the isotherms showed little variation from those of the calcined forms. More obvious differences were found in the PSD curves, which became bimodal for NiAl and Mo/NiAl solids, suggesting the formation of new, larger pores than in their calcined counterparts. Fewer differences were observed in the MoNiAl assay, with a slight upward shift of the PSD.

In their calcined form, the largest specific surface area (S_{BET}) corresponded to the bare NiAl assay (65.2 m^2/g, Table 1). After Mo impregnation, both S_{BET} and V_{pore} decreased by about 30% (Table S1, ESI), indicating a partial blocking of the pores by MoOx, suggesting that below the Mo monolayer loadings, MoOx entities tended to disperse into the smallest pores. Doping the spinel with Mo (MoNiAl assay) had a greater effect on the S_{BET}, which decreased by 48% with respect to NiAl, due to the increase in the average pore size.

After reduction, the S_{BET} decreased significantly for NiAl and Mo/NiAl solids (by 30%), in agreement with their larger pores (Table S1, ESI). Interestingly, MoNiAl retained its S_{BET} upon reduction. The decrease in S_{BET} could be caused by the exsolution of nickel metal (with very low S_{BET}) from the bulk spinel to the surface. Overall, the results indicated that we have successfully prepared mesoporous solids that retain their textural properties upon reduction.

3.2. Structural analysis

The crystalline structure of the solids was examined by XRD and the corresponding diffractograms are shown in Fig. 1. The dominant diffraction peaks of all the calcined solids were consistent with a face centred cubic $NiAl_2O_4$ spinel phase (JCPDS 78–1601). None of the catalysts show a NiO signal, indicating that if present it was highly dispersed or amorphous. For the MoNiAl and Mo/NiAl assays, the absence of any signal from MoOx of any other Mo-containing phase indicated that it was highly dispersed, as expected due to the sub-monolayer Mo loading used [21].

The intensity ratio of peaks (400) to (311) (I_{400}/I_{311}) from the spinel phase represents the extent of occupancy of the substituent ions on the tetrahedral site in the sub-lattice [29]. For the MoNiAl solid, the I_{400}/I_{311} ratio was remarkably reduced compared to the other two solids (0.59 vs. 0.65, Table S2, ESI), suggesting the occupancy of the Mo ions on the octahedral sites in the MoNiAl assay. Based on these results, it could be concluded that the calcined solids have a partially inverted spinel structure [30]. From a structural point of view, the lattice parameter for the calcined NiAl solid (8.005 Å, Table S2, ESI) slightly increased upon Mo addition to 8.025 and 8.029 Å for MoNiAl and Mo/NiAl, respectively (Table S2, ESI) due to its larger ionic radius (Mo^{3+}: 0.68 Å vs. Al^{3+}: 0.83 Å). These results indicated that in the solid obtained from the one-pot synthesis, both Ni and Mo were present in the aluminate spinel matrix.

The diffraction peaks from the spinel phase remained for all solids upon reduction at 700 °C (Fig. 1(B)). This suggests that the employed temperature was insufficient to reduce nickel ions in the stoichiometric $NiAl_2O_4$ lattice. Additionally, new XRD peaks at $2\theta = 44.5°$, 51.9° and 76.5° appeared for all the reduced solids, which corresponded to metallic nickel (JCPDS 01–087-0712). These outcomes conclusively confirmed the exsolution of metallic Ni from the spinel lattice to create supported Ni^0 catalysts. No peaks from molybdenum-containing species were detected, indicating that if they did exist, they were widely dispersed.

Nickel ions exsoluted from the spinel lattice onto the surface upon reduction. Following this, Al^{3+} ions filled the vacant nickel positions, resulting in the formation of Ni-deficient spinel structure. As the ionic radius of Al^{3+} ion is smaller than that of Ni^{2+} (53.5 vs 70 pm), the lattice constant reduced, indicating the formation of γ-alumina (JCPDS 79–1558) [23]. This trend was observed in all catalysts, and the extent of lattice parameter decrease relied on the synthesis method: NiAl and Mo/NiAl decreased by 0.7–0.8%, whereas for MoNiAl, it decreased by 2%.

The crystallite size of the spinel phase was approximately 10 nm for all the calcined solids (Table S2, ESI), indicating that Mo had a negligible impact on the formation of the spinel phase. However, significant variations were observed among the metallic nickel crystal domain sizes (Table 1). Reference NiAl exhibited the most extensive Ni^0 crystallites (12.9 nm), which were reduced by 22–38% with Mo doping. These results indicate that Mo had an effect on the Ni^0 domain size, regardless of the loading method employed. The diminutive size of metallic nickel crystals indicated a significant association of Ni with the spinel phase, which has the potential to stabilize the metallic Ni particles from coalescing [23]. Also, the Ni nanoparticles were firmly embedded into the support substrate, resulting in a strong catalyst-support interaction [31].

3.3. Morphology and microstructure of catalysts

The morphology and microstructure of the reduced catalysts are displayed in Fig. 2. The SEM images (Fig. S3(A), ESI) of the reduced catalysts demonstrate irregularly-shaped and sizeable particles with a densely packed and smooth surface; this is attributable to the elevated temperatures utilized during synthesis. Furthermore, Mo-doped solids

Table 1
Textural properties, Ni^0 crystallite size, and results from H_2-TPR, H_2 chemisorption and NH_3-TPD.

Catalyst	S_{BET} (m^2/g)	d^0_{Ni} (nm)	H_2 uptake TPR_{950} ($mmol/g_{cat}$)	Degree of Reduction[a] (%)	Metallic area (m^a_{Ni}/g_{cat})	Metal/total area ratio (%)	Metal sites density ($sites/nm^2$)	Acid sites density ($sites/nm^2$)	Metal/acid (sites/sites)
NiAl	65.2 (43.4)	12.9 ± 0.4	5.07	77.1	1.38	3.2	0.49	0.71	0.69
MoNiAl	33.6 (34.5)	9.9 ± 0.4	5.49	60.0	1.99	5.8	0.89	1.24	0.72
Mo/NiAl	43.7 (30.1)	7.9 ± 0.3	5.43	61.9	1.90	6.3	0.97	1.42	0.69

In parenthesis, values for reduced forms; [a] TPR_{700}/TPR_{950} H_2 uptake ratio.

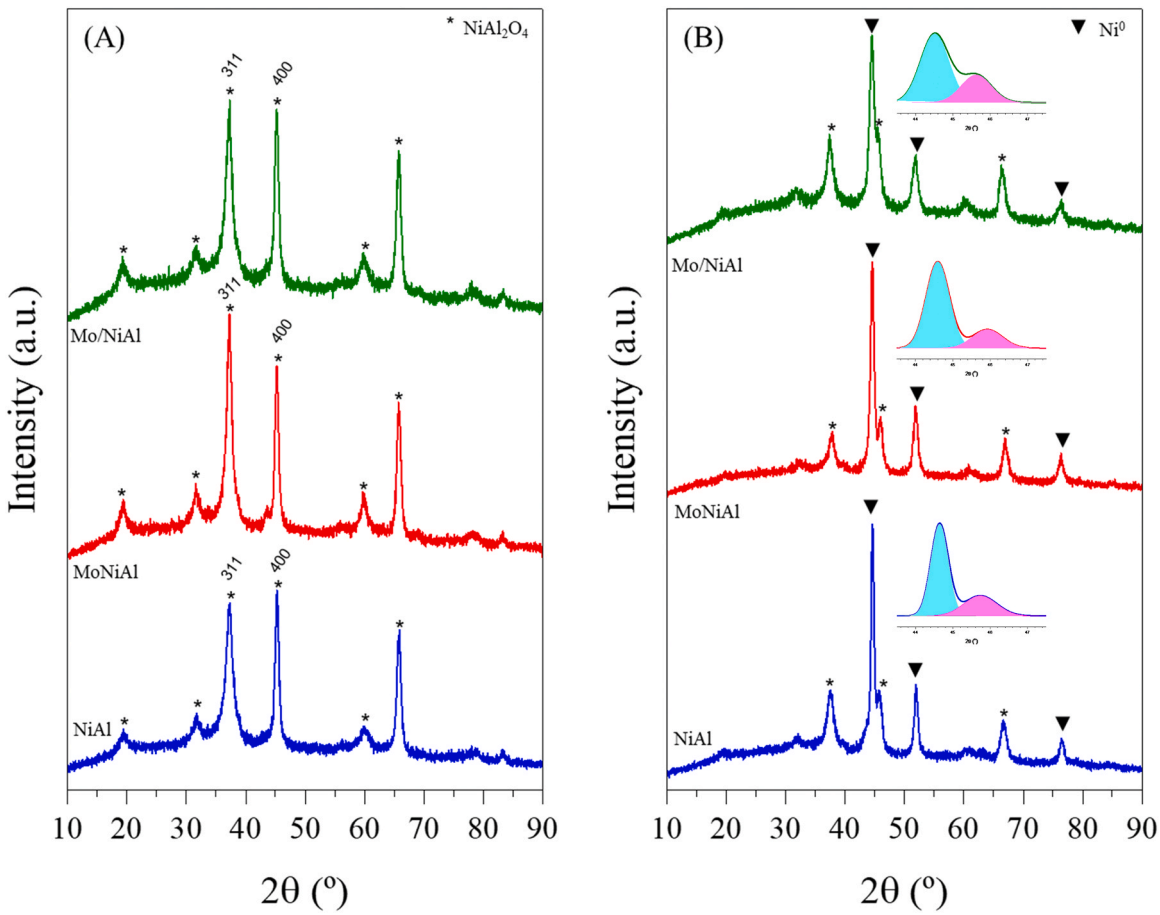

Fig. 1. XRD spectra of the calcined (A) and reduced catalysts (B). Insert: deconvolution of metallic Ni (111) (cyan) and spinel (400) (magenta) peaks.

exhibited a somewhat less compressed structure with less tightly packed edges. By examining HRTEM images (as shown in Fig. 2(A,C,E)), lattice fringes with a measurement of 0.20 nm were observed across all the reduced catalysts, which corresponded to the Ni^0 (111) facet. Furthermore, lattice fringes with measurements of 0.24 nm and 0.47 nm were identified, corresponding to the $NiAl_2O_4$ spinel (311) and (111) facets, respectively. These findings confirmed the presence of Ni^{2+} within the spinel, irrespective of the reduction treatment applied, as indicated by the XRD results. Also, for both Mo-doped catalysts, it was observed that MoO_3 particles (with lattice fringes of 0.38 nm for the (110) facet) were in proximity to the metallic Ni nanoparticles. This proximity suggests the formation of Ni-MoO_X entities resulting from the intimate contact of the metallic Ni particles with partially reduced molybdenum oxide [32]. During the reduction stage, the metal Ni particles emerge from the spinel structure and move to the surface, while the MoOx species that have not been reduced segregate and cover them. This process reduces the metallic particle size, as perceived by XRD, due to the SMSI (Strong Metal-Support Interaction) effect between them, as described in [33].

The STEM images (Fig. 2(B,D,F)) exhibited uniform distributions of Ni and Mo across all catalyst samples. Particle size distribution of Ni was challenging to measure due to the low contrast in the images. Nevertheless, the STEM images indicated that the particle sizes were congruent with the XRD analysis and revealed no agglomerations of Ni particles. Mo mapping indicated that Mo was very dispersed, predominantly in close contact with metallic Ni particles, regardless of the method used. Most of the oxygen was bound to the aluminium (Fig. S4, ESI), in line with the existence of spinel phase. Additionally, there was some oxygen surrounding the Mo and Ni particles, with the latter coming from the passivation preceding the measurement.

3.4. H_2-TPR and characterization of metallic sites

The reducibility of the solids was analyzed through H_2-TPR (Fig. 3). For reference, profiles were included for bulk NiO and MoOx. The TPR_{950} reduction profile of NiAl displayed a large peak (maximizing at 785 ºC), which corresponded to the reduction of Ni^{2+} of stoichiometric $NiAl_2O_4$. The tail on the left indicated various nickel species existence. For instance, the peak at approximately 670 ºC could be attributed to the reduction of Ni species in a nickel-deficient $Ni_{1-x}Al_2O_{4-x}$ spinel [23]. Furthermore, another low-intensity peak was observed, at around 430 ºC, which corresponds to the reduction of NiO that is weakly bonded to the surface. This is due to the formation of a segregated NiO phase, which is not detected by XRD as its quantity is less than 5%. The peaks were deconvoluted (Fig. S5, ESI), indicating that the majority of nickel species was in the form of stoichiometric spinel in NiAl solid (64.6%), which is consistent with the XRD results. The TPR_{950} profile of MoNiAl and Mo/NiAl solids exhibited a similar trend to that of parent NiAl, all of which displayed the same high-temperature peak position. The most significant distinctions were observed in the peak at low temperatures. The Mo/NiAl assay demonstrated the highest contribution of this peak (9.8% vs. 4.5%, Fig. S5, ESI) due to the simultaneous reduction of MoOx species on the surface. This reduction was promoted by the spillover on the nickel particles [34]. For all the catalysts, the relative contribution of Ni in nickel-deficient spinel and stoichiometric spinel was roughly 30% and 65%, accordingly. The minimal involvement of NiO-type species may facilitate to obtain Ni^0 particles with a small crystallite size [35].

Prior to the reaction, the catalysts underwent reduction at 700 ºC for a duration of 2 h. An evaluation of catalyst reduction took place using TPR_{700} (heating from room temperature to 700 ºC and held for 1 h) to measure the level of reduction. It is of note that the TPR_{700} and TPR_{950}

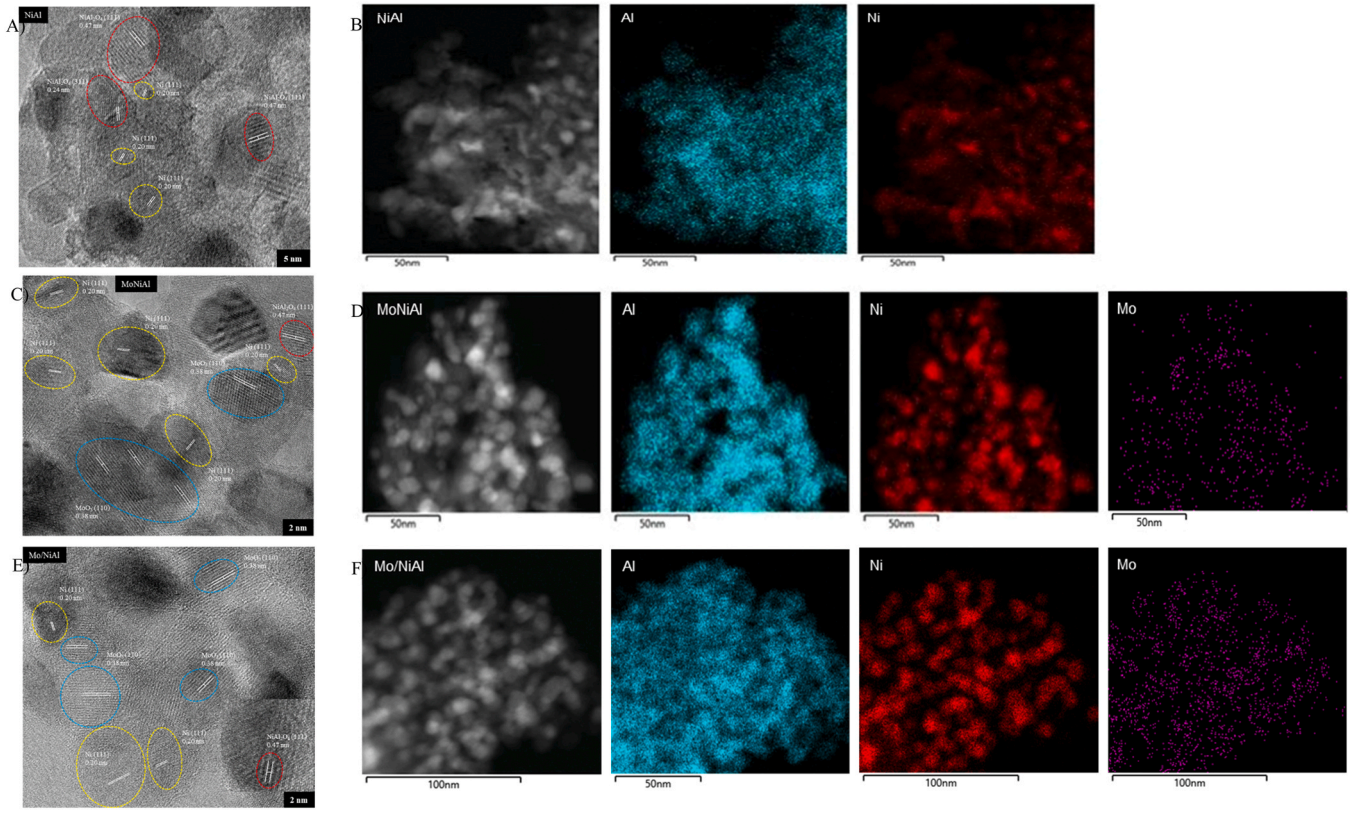

Fig. 2. HRTEM (A, C and E), and STEM-EDX (B, D and F) of the reduced NiAl, MoNiAl and Mo/NiAl catalysts.

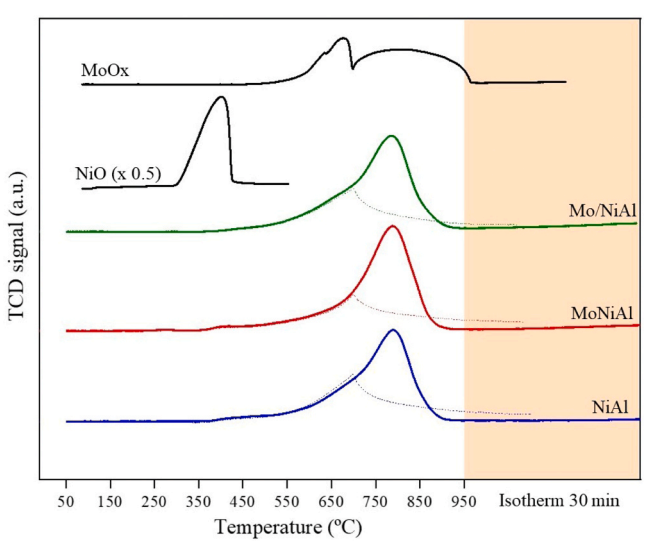

Fig. 3. H_2-TPR profiles of fresh samples. Solid lines: TPR_{950}; dashed lines: TPR_{700}. Profiles for NiO and MoOx are included as a reference.

profiles coincided up to 700 ºC for all samples. According to the TPR_{700} profiles, the treatment applied was able to reduce the free NiO and a portion of Ni^{2+} as non-stoichiometric spinel (observed in the low and intermediate temperature peaks); however, Ni as stoichiometric spinel remained in its oxidized form. Maintaining the nickel aluminate phase improved the resistance of the catalyst to severe hydrothermal conditions when compared to γ-alumina [23]. Table 1 indicates that the reduction degree of nickel in the NiAl catalyst was 77.1%, which decreased by approximately 20% following the addition of Mo. This suggests that Mo impeded the nickel reduction, in line with previous results [36].

As metallic sites are crucial to the hydrogenation/dehydrogenation stages in the aqueous-phase hydrogenolysis of glycerol, the quantity of available metallic sites and their ability to chemisorb and activate H_2 were analyzed using H_2 chemisorption and H_2-TPD, respectively (Table 1). As Mo does not chemisorb hydrogen [37], only Ni^0 was designated to have hydrogen uptake. The bare NiAl solid possessed an active area of 1.38 m^2/g, representing approximately 3.2% of the total surface area. Upon the introduction of Mo, the active area rose by about 40%, despite the reduction degree being lower. Catalysts containing Mo exhibited a twofold increase in the percentage of active area relative to the total area. Such findings were consistent with the diminished metallic nickel domains of Mo-containing solids, as detected by XRD. Various factors may impact the active metal surface. Among these are the amount of Ni atoms that have been exsoluted from the spinel framework during reduction and the coalescence of metallic Ni on the surface. For the NiAl catalyst, there was a reduction of 3.909 mmol Ni^{2+} per gram of catalyst, and it decreased by approximately 15% after Mo-doping. Once the metallic Ni entities were outside the lattice framework, they coalesced to form larger agglomerates due to the high temperature they were subjected to. The XRD analysis showed that the Mo-doped solids had smaller Ni crystal domains, suggesting that Mo hindered the coalescence of metallic Ni particles. This observation was further confirmed by TEM analysis [36]. As such, the process of reducing, adding, and carrying out Mo addition had a significant impact on the accessible amount of metallic nickel.

The H_2-TPD profiles (Fig. S6, ESI) indicate the presence of a single desorption peak, which suggests that the metallic nickel particles on the catalyst surface are homogeneous [38]. The area under the curves matches those obtained by H_2-chemisorption. The absence of a high-temperature desorption peak further indicated the absence of hydrogen located in the subsurface layers or hydrogen that has spilled over onto the surface [39]. Desorption profiles across all tests were comparable, suggesting no significant differences in their potential to

activate H_2. The desorption peaks, with a maximum within the 78–94 °C range, were associated with the weakly chemisorbed desorption of H_2 on greatly dispersed Ni [40]. These metallic sites offer reactive hydrogen species for the hydrogenation process [41].

3.5. Surface acidity

The hydrogenolysis of glycerol in an aqueous phase involves various reactions, including dehydration that is sensitive to the acidity of the surface. This property was measured through ammonia chemisorption (Table 1). The density of acid sites in both Mo-containing catalysts was found to be double of the reference NiAl assay, in line with the acidic attributes of Mo [42]. Among both, Mo/NiAl had the highest density of 1.42 sites/nm^2. Similar results were found in [43], indicating the acidity of MoOx entities. Additionally, highly dispersed Mo species have the potential to function as Brønsted acid sites [44]. Doping the catalyst with molybdenum raises the density of acid sites in accordance with [45].

The balance and proximity between metallic and acid sites can have a significant impact on activity in tandem-type catalysis, influencing the product distribution [46]. As the ratio of metallic/acidic sites was approximately 0.7 for all catalysts, any variation in catalytic performance could be attributed to the intrinsic hydrogenation/dehydrogenation (metal) and dehydrogenation (acid) capacity of each site type.

3.6. Spectroscopic characterization

Fig. 4 (A) illustrates the diffuse reflectance spectra of the calcined solids in the UV–vis NIR region. The deconvolution of the contributions is depicted in (Fig. S7, ESI). The Mo/NiAl assay exhibited the most noticeable absorption band in the UV region, attributed to the metal charge transfer transitions from supported MoO_3 entities on the catalyst surface [47]. The absorption strength within the range of 520–770 nm relates to the d-d electron transition of Ni^{2+}, which shows tetrahedral coordination, with limited input from octahedral nickel at 760 nm. The broad band within the range of 860–1350 nm could be designated to d-d electron transition of Ni^{2+} ions, which are hosted in octahedral sites [48]. Furthermore, the band positioned at 375 nm corresponds to octahedral Ni^{2+} species. The I_{Oh}/I_{Th} ratio of the calcined NiAl and Mo/NiAl samples (Table S2, ESI) was approximately 1.20; for MoNiAl, it slightly increased to 1.34, in line with XRD results. The doping effect of Mo was further demonstrated by the variation in band-gap energy (Eg) of the Mo-doped catalysts compared to NiAl (Table S2, ESI). Consistent with expectations, impregnation of Mo resulted in less structural modification than one-pot addition. These findings provide evidence of the inclusion of Mo within the crystal lattice, particularly in the Mo/NiAl assay.

Further analysis of the solids was conducted using Raman spectroscopy (see Fig. 4(B)). The Raman spectrum of NiAl exhibited three bands at approximately 370, 590, and 800 cm^{-1}, which were associated with the Eg, T2g, and A1g modes of the spinel phase, respectively [30]. The absence of Raman lines from NiO (at around 500 cm^{-1}) indicated that it was highly dispersed, consistent with the XRD results [48].

When 1 wt% of Mo was impregnated onto NiAl (solid Mo/NiAl), the Raman spectrum became more complex, with new, broad lines merging at high frequency. While the Eg and T2g Raman lines were generally preserved, there were no separate bands identified from Mo species. The intense and broad peak within the range of 700–950 cm^{-1} was caused by the A1g mode lines of the spinel as well as the bridging Mo-O-Al stretch line [49]. The 980 cm^{-1} band is likely attributable to the symmetric stretch of well-dispersed MoOx species on the surface [50]. These monomer species are the most prevalent type for supported Mo solids at low Mo coverages [51]. The Raman spectrum of MoNiAl solid retained the Eg and T2g Raman lines found in NiAl spinel. The structured signal within the range of 650–1010 cm^{-1} possibly corresponds to Mo in an aluminium environment [49]. Moreover, the low intensity of the 980 cm^{-1} band indicates lesser MoOx species at the surface in the MoNiAl sample.

The bands characteristic of spinel at 370 and 590 cm^{-1} were perceptible yet weakened on the reduced catalysts (Fig. S8(A), ESI). This indicates that the H_2 treatment at 700 °C did not fully reduce nickel as confirmed by XRD and H_2-TPR. Additionally, the peaks from Mo were retained by both Mo-containing catalysts, inferring that it remained oxidized.

XPS was used to assess the surface composition and oxidation state of various elements. XPS data for the Ni 2p3/2 and Mo 3d core levels of the calcined and reduced catalysts are presented in Fig. 5. The binding energies (BE) of the Ni 2p3/2, O 1 s, Al 2p, and Mo 3d core levels are summarized in Table S3(ESI). Additionally, Fig. S9(ESI) provides detailed XPS spectra for the O 1 s and Al 2p core levels.

The Ni 2p3/2 scan of all the calcined solids revealed comparable peak intensities due to the same Ni loading. The spectra comprised of two parts in the ranges 855.5–855.9 eV and 861.6–861.9 eV, respectively, corresponding to the primary and shake-up satellite peaks, both

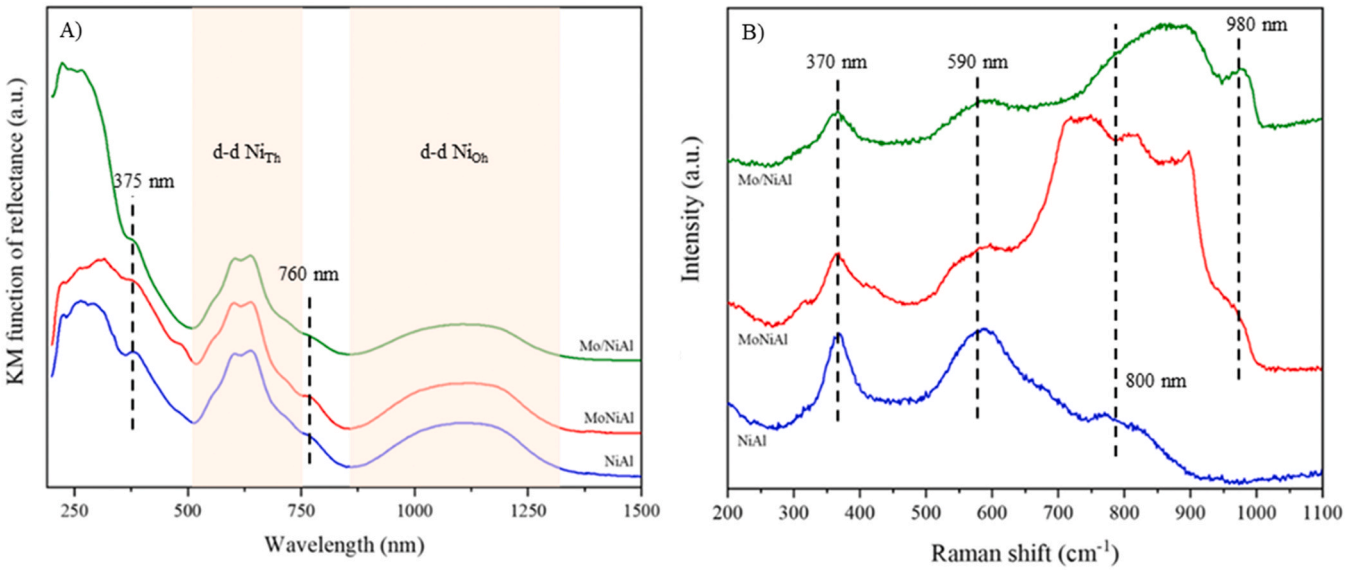

Fig. 4. (A) DRS UV–vis NIR spectra and (B) Raman spectra of the calcined solids.

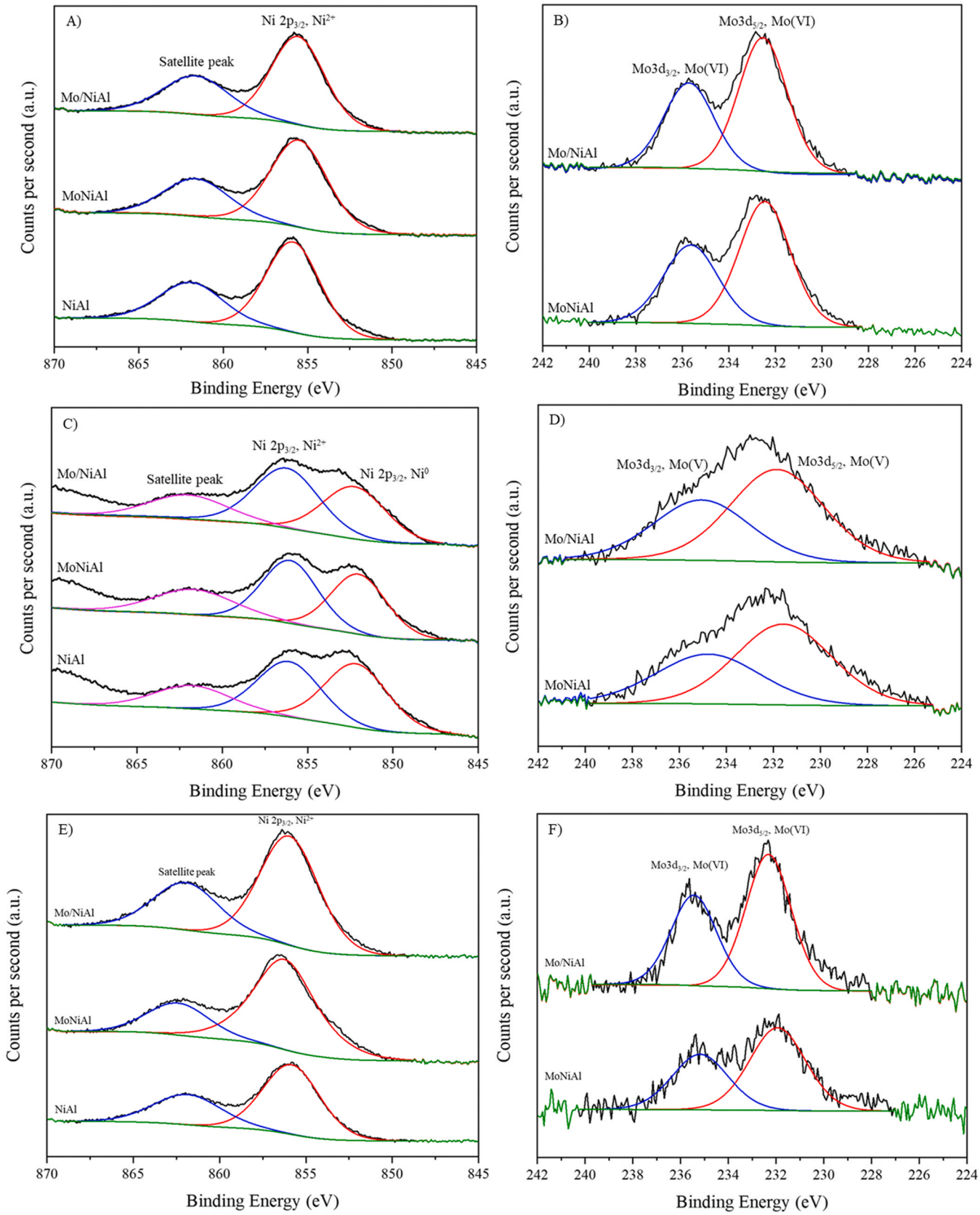

Fig. 5. XPS spectra of Ni $2p_{3/2}$ and Mo 3d in their calcined (A, B), reduced (C, D), and (E,F) spent forms.

characteristic of Ni^{2+} species [52]. This signifies that the freshly calcined solids had completely oxidized nickel. The position of the main peak on the surface was ascribed to Ni^{2+} species similar to $NiAl_2O_4$, as supported by H_2-TPR and XRD findings. The main peak's position downshifted by 0.3–0.4 eV in Mo-containing solids, indicating that the nickel species received an electron density from highly oxophillic MoOx [53]. The findings confirm a substantial interaction between Ni and Mo, which was observed via electron microscopy. Although the H_2-TPR technique identified surface NiO species, their low concentration within a narrow binding energy range disallowed their resolution in the spectra. These results suggest that most of the surface Ni strongly interacted with the alumina and molybdenum surroundings in all the calcined solids.

Almost identical Mo 3d spectra were obtained for both solids containing Mo, regardless of the method used to introduce Mo. The spectra were analyzed and categorized into two peaks, which correspond to Mo 3d5/2 and Mo 3d3/2 at 232.5 eV and 235.6 eV, respectively, for both solids. This finding indicates that Mo^{6+} species are present only at the surface [54]. The species was not detected using XRD because of high dispersion and/or molybdenum embedded in spinel structure.

The O 1 s XPS spectra for all calcined solids exhibit a symmetrical, relatively broad shape (FWHM 2.9–3.1 eV) due to the presence of oxygen-containing species on Ni, Al, and Mo. The peaks centred at 530.8–531.1 eV could be attributed to the oxygen anion in the $NiAl_2O_4$-like structure [55]. The involvement of Mo causes the BE downshift by 0.2–0.3 eV, which could be attributed to the O-metal interaction weakening. The small energy separation between Al 2p and Ni 3p peaks causes partial overlap (see Fig. S9(B), ESI). All the calcined assays indicated the presence of $NiAl_2O_4$, with a main peak at 74.2 eV [56]. Additionally, Ni 3p core level spectra of Ni^{2+} species gave rise to an extra component at 68.3 eV, in line with the findings in [57].

Upon reduction, there was a significant variation in the Ni 2p3/2 spectra compared to the calcined forms, particularly in the main peak. Deconvolution indicated two contributions, one corresponds to spinel-like Ni^{2+} species (856.0–856.2 eV range), whilst the other corresponds to Ni^0 (852.0–852.3 eV range) [58]. In the spectra of the calcined forms, the second contribution was not observed, which indicates that the reduction caused the formation of metallic nickel at the surface. The binding energy (BE) of the main peak shifted up by 0.2–0.6 eV when compared to the calcined forms, indicating the presence of Ni-defective spinel. The shake-up satellite peak at approximately 861.8 eV remained unchanged in calcined assays, which suggested a fraction of oxidized nickel, in agreement with H_2-TPR [52].

There were slight changes in the Mo 3d spectra for the reduced solids compared to those of calcined assays with less resolution of 3d5/2 and 3d3/2 bands. The bands exhibited a downshift of 0.7–0.85 eV in comparison to those of the calcined forms and were assigned to Mo^{5+} species [59]. The contribution of metallic Mo was not identified, despite the high reduction temperature employed (700 °C). For Mo/alumina and Ni-Mo/alumina prepared through impregnation, metallic Mo was detected upon reduction at 600 °C [60]. This indicates that for our catalysts, the reduction of Mo species was impeded by a strong interaction with Al and Ni species, which is consistent with Raman findings.

The form and peak position of the O 1 s XPS spectra of all the reduced solids were essentially identical to those of the calcined solids (Fig. S9 (A), ESI). Nevertheless, there was a decrease in intensity, indicating a reduction of oxygen, in agreement with the oxygen eliminated by hydrogen. Moreover, the Al2p peak position remained constant, although the rise at a higher binding energy demonstrated an increase of Al ions occupying Oh positions. The Al2pNi3p spectra obtained from the reduced catalysts (Figure S9(B), ESI) indicated a supplemental contribution (at lower binding energy, approximately 66.1 eV) ascribed to metallic Ni, thus confirming the reduction of nickel species present on the surface.

The surface atomic distribution of Ni, Mo, Al and O species was quantified using the area under the various peaks (see Table 2). In all the solids, the proportion of oxygen in the surface was approximately 60% (i.e. O/Me around 1.5). In comparison to the NiAl counterpart and regardless of the method used for Mo addition, both the Mo/Ni and Ni/Al ratios diminished. The latter suggests the presence of a nickel-deficient aluminium-rich phase on the surface, which is consistent with H_2-TPR findings. The surface reduction degree, measured by the ratio of Ni^0 to total Ni, decreased after the addition of Mo, indicating that the reducibility of nickel is hindered by Mo, which is consistent with H_2-TPR. Moreover, the Ni/Al ratio at the surface of the Mo-doped catalysts was reduced by approximately 30%. This could be attributed to the decoration of Ni on the surface by MoOx, as seen by electronic microscopy [32]. A reduction in Ni/Al ratio was demonstrated to a lesser extent in the NiAl assay (by 17%), corroborating previous findings [53]. Upon reduction, Mo/Al ratio decreased in all catalysts. Meanwhile, the Mo/Ni ratio only slightly differed from its calcined counterparts, suggesting MoOx was redistributed during the reduction process.

3.7. Catalytic performance experiments

Catalytic testing was conducted to study glycerol hydrogenolysis with hydrogen in-situ produced by APR (one-pot APR-HDO). The experiment took place using a fixed-bed up-flow reactor under the temperature and pressure of 235 °C/45 bar, without any extra hydrogen addition. The obtained data is for 4 h TOS, as no significant deactivation was observed during this time period.

Control experiments using calcined NiAl and bare γ-alumina (not shown) demonstrated very low activity ($X_{Gly} < 5\%$), highlighting the fundamental importance of the metal function. NiAl showed the highest glycerol conversion rate (81.7%, Fig. 6(A)) followed by MoNiAl and Mo/NiAl (77.2% and 69.1%, respectively). Regarding the carbon distribution in the liquid products, Y_{Liquid} was observed to be NiAl (30.8%) < MoNiAl (44.4%) ≈ Mo/NiAl (47.7%). It is concluded that Mo-doping had a positive effect on the yield of liquid products, as Y_{Gas} displayed an opposite trend, in line with [22,61]. In all cases involving the catalysts, Y_{Liquid} and Y_{Gas} combined were found to be below X_{Gly}. The reason behind this was products getting adsorbed on pores or carbon deposits, causing a C-balance of around 90% in the worst-case scenario. The level of deoxygenation (DOD) for NiAl was 58%, which decreased for the Mo-doped catalysts, aligning with the trend of glycerol conversion.

The gas product for all catalysts consisted mainly of CO_2 (as the principal product), H_2 and CH_4, which accounted for approximately 85–95% of all gases (on a dry basis) (see Fig. 6(B)). Compared to other catalysts, Mo/NiAl production of C2 + alkanes increased (C2 +: 13.4% vs. 5%). CO was obtained in lower concentrations (below 3.3%) for all catalysts. The H_2/CO_2 ratio decreased in the following order: NiAl (0.74) > MoNiAl (0.70) >> Mo/NiAl (0.36). These ratios were much lower

Table 2
Composition at the surface, and at bulk (atom/atom).

Catalyst	Surface					C/Me*	Bulk	
	Ni/Al	Mo/Al	Mo/Ni	O/Me	Ni^0/Ni		Ni/Al	Mo/Ni
NiAl	0.367/0.303/0.259	0/0/0	0/0/0	1.50/1.22/1.37	0/0.433/0	0.071	0.495	0
MoNiAl	0.376/0.256/0.215	0.039/0.022/0.010	0.104/0.09/0.052	1.58/1.20/1.63	0/0.381/0	0.045	0.493	0.019
Mo/NiAl	0.370/0.265/0.323	0.040/0.025/0.016	0.109/0.10/0.056	1.49/1.21/1.75	0/0.373/0	0.067	0.492	0.019

Calcined/reduced/spent; Me=Ni+Mo; * C sp^3 in spent catalysts.

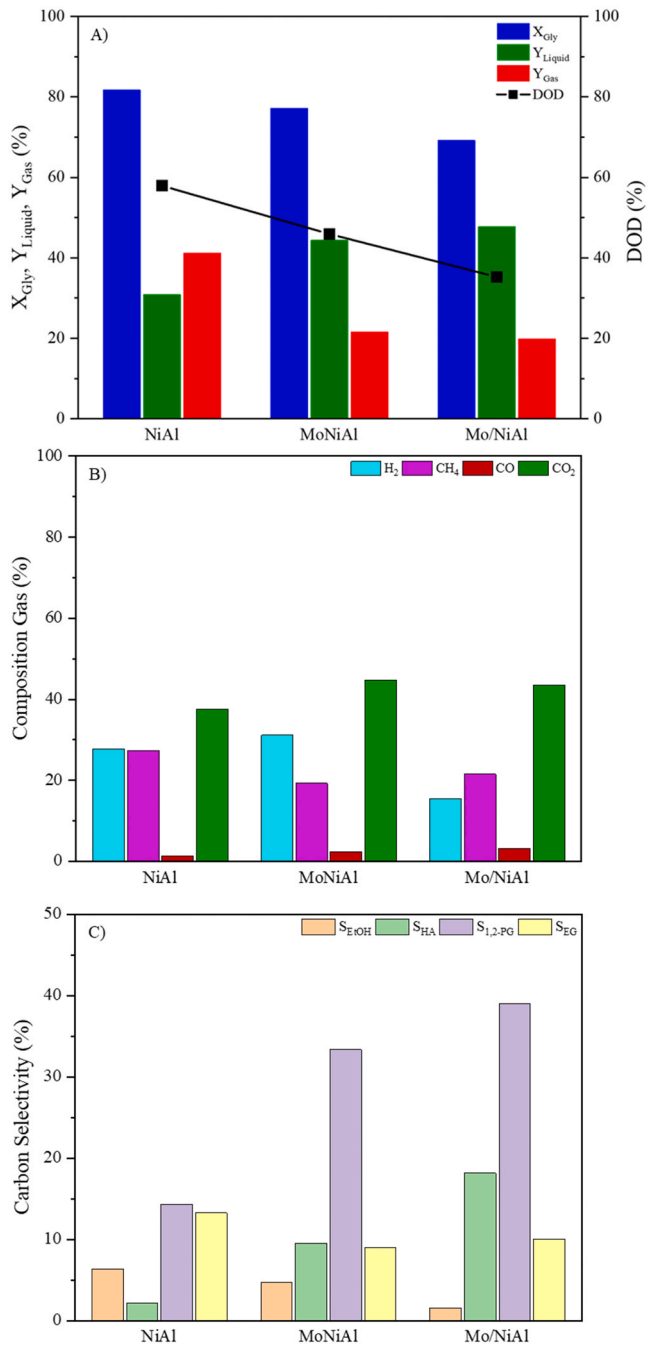

Fig. 6. (A) Activity and yields in the one-pot APR-HDO reaction; (B) Composition of the gas products; (C) Carbon selectivity to liquids. Reaction conditions: 235 ºC/45 bar, WHSV = 12 h^{-1}, data at 4 h TOS.

than the ideal APR (2.33) and suggested in-situ consumption of hydrogen produced by glycerol APR. All catalysts produced significant amounts of methane (20–27%). Ni is a metal with a recognized capacity for CH_4 production through CO/CO_2 hydrogenation due to its ability to form subcarbonyl species [62]. The NiAl catalyst achieved a ratio of H_2/CH_4 of approximately 1, which was then followed by a dissimilar trend upon Mo-doping. The ratio increased to 1.62 for MoNiAl and decreased to 0.74 for Mo/NiAl catalysts.

The methane production capabilities of the catalysts were evaluated using the $CH_4/(CO+CO_2)$ ratio. The reference NiAl catalyst demonstrated the highest ratio (0.69) among all the catalysts tested. However, the ratio decreased to 0.46–0.41 for the Mo-containing catalysts, indicating that the Mo-doped catalysts were less efficient in CO/CO_2 hydrogenation. This deduction is in line with [63]. The CO/H_2 ratio exhibited variability as follows: 0.047 (NiAl) is lower than 0.075 (MoNiAl), and significantly lower than 0.209 (Mo/NiAl), indicating that the addition of Mo through impregnation has a detrimental effect on the Water-Gas Shift (WGS) reaction. Authors from [64] found no improvement in WGS activity through Mo-doping for $Fe_{2.4}Ce_{0.3}Mo_{0.3}O_4$ type spinels.

Some of the carbon supplied as glycerol was acquired in liquid form. In accordance with previous literature [14], the liquid-phase hydrogenolysis of glycerol on bifunctional catalysts includes three main pathways involving dehydration, dehydrogenation, and hydrogenation reactions [15]. Path A involves the successive dehydrogenation/decarbonylation (C-C scission) occurring on metal sites, which produces CO and ethylene glycol (EG). These products can be further processed. The carbon loss from the products generated along this pathway classifies them as degradation products [65]. Paths B and C involve the dehydration process (C-O scission) occurring on acid sites of primary hydroxyl (Path B) yielding hydroxyacetone (HA) or on secondary hydroxyl (Path C) producing 3-hydroxypropanal, which are subsequently hydrogenated (on metal sites) resulting in the formation of 1,2-propylene glycol (1,2-PG) and 1,3-PG, respectively. Further steps of dehydration or hydrogenation lead to the production of mono-alcohols and alkanes. Path B is preferred for Lewis acid sites whereas Brønsted acid sites are inclined towards Path C [66]. Path A is the preferred route for hydrogen production while paths B and C are preferred for hydrogenolysis purposes [67]. Within this reaction scheme, WGS is utilized for the conversion of CO into CO_2 and hydrogenation is used for the conversion of both CO and CO_2 into CH_4. To promote hydrogenolysis reactions, the hydrogenations of CO and CO_2 must be inhibited.

Focusing on the liquid products (Fig. 6(C)), the addition of Mo substantially altered the distribution of products. The primary liquid products were 1,2-PG, EG, HA, and ethanol, accounting for over 95% of all liquid products. Methanol, acetone, acetaldehyde, and propanols were also observed as minor products. The low yields of propanols suggest that the hydrogen produced in-situ by APR selectively hydrogenates HA and avoids over-hydrogenation [68]. No products resulting from C-C coupling were detected. Consequently, both paths A and B were followed, as indicated by the obtained products. Notably, none of the catalysts produced primary products from Path C, implying that the acid sites dehydrated the primary hydroxyl from glycerol in preference. It is likely that the high-temperature reduction undergone by catalysts decreased the Brønsted acidity characteristic of molybdenum [69], which is low in itself due to the low loading of Mo. Initially, the selectivity to HA and PG appeared to increase with Mo doping, at the expense of EG and ethanol. The increase in acid sites density after Mo-doping (Table 1) was attributed to the observed trend, as both HA and PG were found to result from Mo-ascribed acid sites that underwent C-O bond scission [66]. The stronger Mo-O bond in MoOx entities was also deemed to facilitate oxygen removal [70]. Additionally, the higher acid sites density of Mo/NiAl, compared to MoNiAl, led to a greater increase in selectivity towards HA and PG products. Among all of the catalysts tested, the Mo/NiAl catalyst demonstrated the greatest selectivity towards 1,2-PG at 39%. Likewise, 1,2-PG exhibited the highest yield when using Mo-doped catalysts, reaching approximately 27% as shown in Table 3.

Table 3 summarizes the yields and distribution of liquid products. The STY_{PG} rates for 1,2-PG were 0.74, 1.12 and 1.23 min^{-1} for NiAl, MoNiAl and Mo/NiAl, respectively. These rates showed an linear correlation with the density of metal sites (Table 1). The production of 1,2-PG occurred through a series of reactions involving glycerol dehydration and subsequent hydrogenation of the resulting C=O bond, thereby involving both metallic and acid sites. The 1,2-PG/HA ratio varied as follows: NiAl (6.7) was found to be less effective than MoNiAl (3.5) and Mo/NiAl (2.2), with selectivity being inversely related to metallic site density as shown in Table 1. The results obtained suggest that acid-catalyzed dehydration played a crucial role in our catalysts [65]. The

Table 3
Yields and distribution of liquid products according to functionalization.

Catalyst	$Y_{1,2\text{-}PG}$ (%)	$Y_{1,2\text{-}PG}/Y_{HA}$	STY_{PG} (min^{-1})	C-O/C-C	Product category (%)			
					Aldehydes	Ketones	Monoalcohols	Diols
NiAl	11.7	6.7	0.74	1.7	0.1	5.6	21.3	73.0
MoNiAl	25.8	3.5	1.12	5.3	0.1	16.4	9.8	73.7
Mo/NiAl	27.0	2.2	1.23	5.9	0.1	26.2	2.7	71.0

selectivity of EG in Path A products ranged from 8–13%, which was twice that of ethanol (generated from hydrogenolysis of EG) for all catalysts except Mo/NiAl, where it was boosted seven-fold. The greater reactivity of glycerol towards 1,2-PG compared to that of EG towards ethanol may be attributed to the more facile hydrogenolysis of the C-O bond in substrates having higher numbers of OH groups. In Rh-MoOx catalysts, the selectivity in hydrogenolysis reactions is, indeed, influenced by the structure of MoOx particles [71]. The selectivities obtained suggest that dehydration of glycerol is the rate determining step for the production of HA while the hydrogenation of HA is the rate-determining step for the production of 1,2-PG.

The primary liquid products were categorized into two groups: C-C scission products (EG) and C-O scission products (1,2-PG, HA, ethanol). The obtained C-O/C-C ratios demonstrated the following trend: NiAl (1.7) $<<$ MoNiAl (5.3) $\approx$ Mo/NiAl (5.9). The carbon selectivity of the liquid products was mainly dominated by the C-O scission products, particularly for Mo-doped catalysts. This highlights the effectiveness of Mo for hydrogenolysis reactions [67,69,72]. The liquid products were categorized into four distinct groups based on their chemical functionality: aldehydes, monoalcohols, diols, and ketones (Table 3). The diols category was found to be the predominant one for all catalysts with a majority of over 70% of the liquids. A trade-off was observed for the distribution of ketones and monoalcohols, with Mo-doped catalysts promoting the former due to their enhanced dehydration ability.

The duration of contact between the reactants and catalyst significantly affects the distribution of products [72]. Therefore, the influence of contact time was investigated using WHSV as a variable (increasing WHSV results in a shorter contact duration), with feedstream flow rates ranging from 0.05–0.3 mL/min over 0.5 g of catalyst to achieve a WHSV range of 6–36 h^{-1} (see Fig. 7).

Firstly, it should be noted that the three catalysts achieved similar conversion values at WHSV = 12 h^{-1}, allowing for meaningful selectivity comparisons. Fig. 7A indicates that lower space velocities led to higher glycerol conversion rates for all catalysts due to the availability of more active sites for the reactants. Additionally, both Y_{Gas} and Y_{Liq} decreased with WHSV within the studied ranges (not shown), coinciding with other research findings [73,74]. Moreover, the selectivity towards 1,2-PG greatly relied on WHSV for all the catalysts, while for the NiAl catalyst, this effect could only be analyzed for glycerol conversions above 50%. The $S_{1,2\text{-}PG}$ of this catalyst demonstrated a decline in tandem with glycerol conversion due to the significant surge of Y_{Gas} (reaching up to 89% for 6 h^{-1}). In contrast, Mo-doped catalysts evinced a boost in $S_{1,2\text{-}PG}$ with X_{Gly}, suggesting a more effective disposition of their metallic/acidic sites. Fig. 7C illustrates that for all catalysts tested, the degree of deoxygenation (DOD) increased with X_{Gly}, due to the increase in the contact time. This can be attributed to the enhancement of sequential dehydration/hydrogenation reactions resulting from boosted availability of catalyst active sites (acidic and metallic).

Table 4 presents a comparison of significant glycerol hydrogenolysis performances in continuous reactors with in situ hydrogen to date. Although a high WHSV was utilized, our MoNiAl catalyst's outcomes in yield and selectivity for 1,2-PG match those of other catalysts, particularly those containing copper, commonly used for C-O hydrogenolysis [13]. The MoNiAl and MoNiAl catalysts used in this work produced some of the highest STY_{PG} values reported in the literature for glycerol hydrogenolysis without external hydrogen.

3.8. Characterization of spent catalysts

The spent catalysts were subjected to post-reaction characterization (4 h TOS, at 235 °C and 45 bar) to gain insight into the changes that had occurred. Table 5 summarizes the principal physico-chemical features of the spent catalysts.

The N_2 isotherms (Fig. S10(A), ESI) showed minor variations when compared with those of the reduced counterparts, suggesting that the spent catalysts retained their mesoporous structure. After being used for 4 h in glycerol hydrogenolysis, the pore size distribution of NiAl and Mo/NiAl underwent notable changes. This occurred as the larger pores, which were generated during reduction, vanished, resulting in a PSD that was similar to their calcined forms (Table S1, ESI). Consequently, there was a marked increase (by 38–77%) in the surface area of these spent catalysts (Table 5). MoNiAl assay was found to be more structurally stable in hydrothermal environments, exhibiting only an 8% increase in surface area, and an almost identical PSD to that of its reduced form (Figure S10(B), ESI). These findings suggest that the addition of molybdenum at the bulk level enhances the hydrothermal stability of the spinel-derived catalyst. The rise in surface roughness of the spent catalysts, as seen through SEM (Fig. S3(B), ESI), provides evidence for the alterations in textural features.

The XRD spectra of the spent catalysts (Fig. 8 A) were similar to the reduced forms, exhibiting characteristic peaks from spinel and metallic nickel. The only discernible difference was observed in the spinel XRD peaks, which were slightly downshifted in 2θ. Consequently, there was an increase in the lattice parameter of the spent catalysts in comparison with the reduced forms (Table S2, ESI). The presence of metallic nickel was confirmed at a bulk level due to the persistence of its signals and the absence of NiO peaks. In previous works, we have observed that the outer layers of nickel oxidize during glycerol APR [23], which suggests NiO may also be present, albeit at levels too low to detect via XRD. The proportion of signal intensity from Ni^0 to spinel significantly decreased in comparison to that of the reduced catalysts (a decrease by 63%, 58% and 29% for NiAl, MoNiAl and Mo/NiAl, respectively). This indicates a reduced presence of metallic nickel on the surface of the catalyst. However, the percentage of oxidized Ni has to be minimal, as the stable yields of reaction products throughout the 4-hour reaction period.

The spent catalysts were also noted for exhibiting an insignificant coalescence of metallic nickel (Table 5), which increased by less than 10% for all the catalysts. Since there was only minimal growth in nickel particles observed for all of the spent catalysts, it can be concluded that nickel sintering has only a marginal impact on the deactivation of the catalysts. The lack of any XRD peak attributed to Mo-containing species suggests a high level of dispersion in the spent catalysts. Since the performance of the catalysts remained nearly constant throughout the four-hour reaction, it can be inferred that the metal oxidation occurred during the initial contact with the liquid stream.

It is worth noting that diffraction peaks were not observed from carbon and hydrated phases of alumina (such as boehmite) in spent catalysts. As carbon was detected on spent catalysts through other techniques (discussed below), it indicates that it was likely of small size or amorphous nature and thus not detectable by XRD. It is worth mentioning that there were no peaks observed from boehmite, which coincides with the Raman spectra (Fig. S8(B), ESI). Boehmite formation is frequently observed in glycerol hydrogenolysis in aqueous phase using catalysts derived from nickel aluminate spinel synthesized through co-

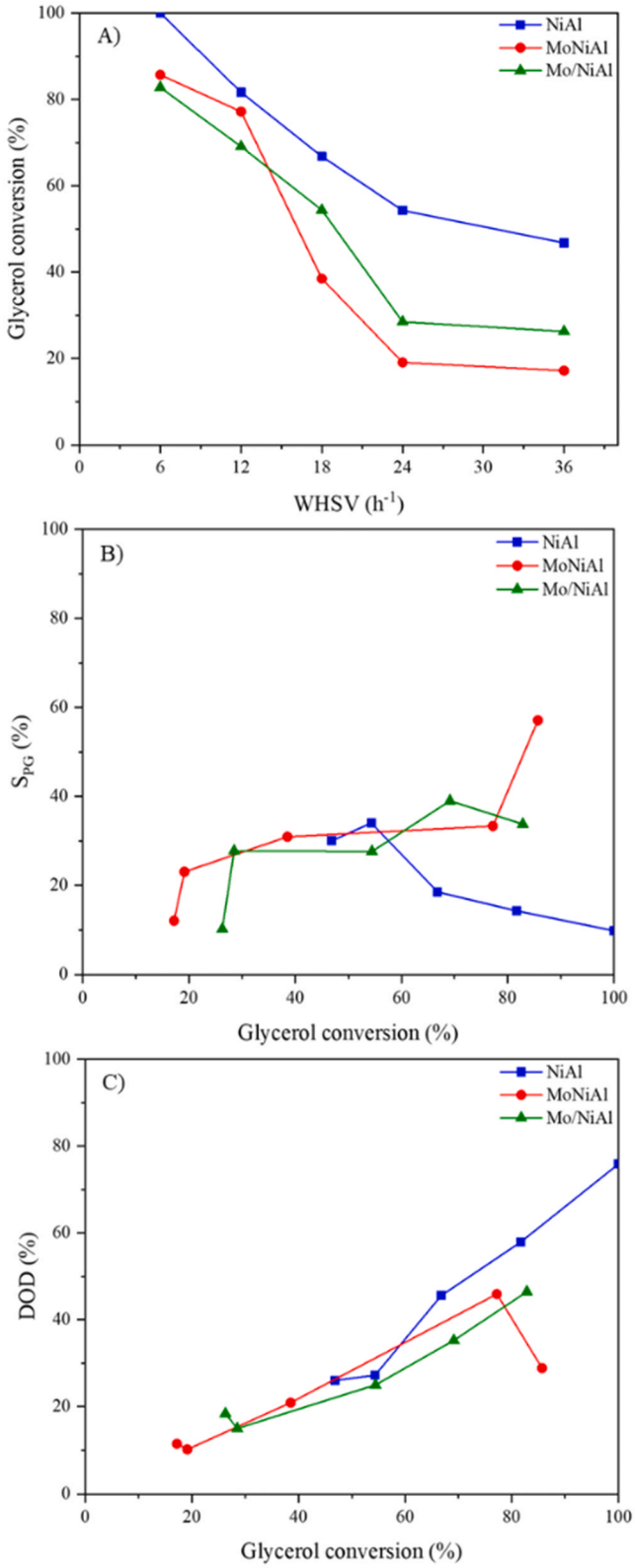

Fig. 7. Effect of WHSV on X_{Gly} (A), S_{PG} vs X_{Gly} (B), and DOD vs X_{Gly} (C).

precipitation [23,27]. Therefore, it can be inferred that the use of the sol-gel method with citric acid as a precursor produced a catalyst that, after reduction, inhibited the hydration of alumina.

Deactivation due to leaching has been extensively reported in the treatment of aqueous-phase biomass [80,81]. Therefore, an aliquot of the liquid product accumulated over four hours was analyzed by ICP-MS, and the respective leached quantities were presented in Table 5. The overall leaching was below 0.5%, with Ni showing the highest extent. Doping with Mo increased the Ni leaching by one order of magnitude, with a more pronounced effect observed for the Mo/NiAl catalyst. Additionally, Mo also leached, particularly in the MoNiAl assay. The findings indicate that aluminium leaching was negligible, possibly due to the capacity of hydrated alumina to leach-off and re-deposit on the catalyst's surface, generating additional porosity in the solid [82], which could explain the increase in S_{BET} after usage. Possible causes of leaching include the formation of corresponding hydroxides, with increased solubility [83], which are favored by the acidity of the medium, or chelating to form soluble complexes with organic compounds [84]. The findings suggest that producing nickel catalysts through the reduction of aluminate spinel generates Ni particles that are firmly attached to the support due to SMSI, resulting in greater resistance to leaching [84].

After accounting for the leached metal and the crystallite size of the spent catalysts, we have estimated a percentage reduction in the metallic area. This variation ranges from 5.3% (Mo/NiAl) to 20% (MoNiAl), which is in accordance with the stability of catalysts during the 4-hour reaction period.

Spent catalysts were evaluated using XPS to provide insight into the oxidation state and chemical surroundings of the elements on the catalyst surface (Fig. 5 and Table S3, ESI). The metallic Ni peaks were not observed for all catalysts as a result of the oxidation of the surface caps, due to the pyrophoric nature of nickel, during the transfer of the sample from the reactor to the XPS chamber. However, appreciable variations were noted in the Ni 2p 3/2 spectra when compared to the calcined samples, particularly in Mo-containing assays, as both the main and satellite peaks showed an upward shift (Table S3, ESI), suggesting the Ni-defective spinel remained. The shift of the Ni peak is consistent with the presence of $Ni(OH)_2$ [85] which could be formed in the outmost layer of metal particles as preliminary stage for leaching. Correspondingly, the Mo 3d5/2 bands of the spent catalysts shifted 0.4–0.5 eV to higher BE as opposed to the reduced forms and were assigned to Mo^{6+} species, indicating that surface molybdenum oxidized during the reaction.

The Al 2p peak position in the spent catalysts (Table S3, ESI) varies between the reduced and calcined ones, particularly in the catalyst Mo/NiAl. In this sample, there was a marginal shift of the Al 2p peak towards higher BE (about 0.1 eV), which could be due to boehmite [86]. The peaks of O 1 s (Table S3, ESI) exhibit higher BE in comparison to the reduced samples (0.2–0.5 eV), consistent with both the presence of Ni $(OH)_2$ and C═O carbon species.

The C 1 s region spectra of the used catalysts (Fig. S11, ESI) illustrated a main peak at approximately 284.5 eV, along with a slight shoulder at approximately 288.3 eV. The main peak could be assigned to aliphatic carbon, as a result of the presence of reaction products that had been adsorbed in the catalysts pores. The shoulder, constituting around 8–11% of the overall area, may be assigned to sp^2 hybridized carbon (-C═O) [87]. After performing XPS measurements on the spent catalysts, they were reduced in situ at 700 °C. This treatment resulted in the persistence of only the carbon peak at 288.4 eV at levels below 1 at% of C (not shown), indicating that the elimination of coke is possible through treatment with H_2 at a temperature of 700 °C [88].

After four hours of reaction, the Ni/Al ratio on the catalyst surface decreased by approximately 15% for both the NiAl and MoNiAl assays. These findings are consistent with the re-deposition of boehmite in the spent catalysts, contributing to the enrichment of aluminium on the surface. However, the ratio increased by 22% for the spent Mo/NiAl catalyst, probably due to its highest leaching of aluminium. For both Mo-containing catalysts, the surface content of Mo decreased with respect to both Al (by 36–54%) and Ni (by 50%). The surface of all the spent catalysts was enriched in O, as compared to the reduced assays. This observation is consistent with the oxidation of the surface layer of nickel and the presence of O-containing carbonaceous deposits. In general, the

Table 4
State of the art of catalysts for the glycerol hydrogenolysis with water as solvent and without external hydrogen. S, Y and STY_{PG} are referred to 1,2-PG.

Catalysts	Reactor	T (°C)	P (bar)	Glycerol/Water (g/g)	WHSV (h^{-1}) or W_{cat}/W_{gly} (g/g)	Time (h) or TOS (h)	X_{Gly} (%)	S (%)	Y (%)	STY_{PG} † (min^{-1})	Ref.
65%Ni/SiO_2-Al_2O_3	Batch	240	33.5 (N_2)	1/10	0.25	4	75	29	22	n.d.	[75]
0.5Cu/MgO	Batch	200	Autogenous	2/10	0.1	23	55	68	37.4	n.d.	[76]
Ni/CeO_2	Batch	230	20 (N_2)	1/10	6.31/1	1	54.3	18.6	10.1	n.d.	[77]
5%Pt/C	Batch	160	35(N_2)	1/10	1/15	2	46.9	23.1	10.8	n.d.	[78]
5%Ru/Al_2O_3 + 5% Pt/Al_2O_3*	Batch	220	41 (N_2)	1/10	0.25/3	6	42.8	45.8	19.6	n.d.	[24]
PtSn0.4	Batch	200	Autogenous	1/10	0.25	2	49	63.3	31	n.d.	[79]
20%CuNi/ZSM-5	Fixed bed	250	40	1/10	2	6	87	31	27	0.12	[26]
20%CuNi/Al_2O_3	Fixed bed	250	40	1/10	2	6	82	29.3	24	0.03	[26]
28Ni/Al_3Fe_1	Fixed bed	227	34	1/10	3	3	42.3	51	21.6	1.41	[27]
CuO/$CuAl_2O_4$	Fixed bed	220	20	2/10	1.53	6	90	55	49.5	0.93	[25]
Ni/Cu/TiO_2	Fixed bed	230	35	0.5/10	4.6	1	30.3	32.7	10	0.09	[9]
Cu-Ni/MgO-Al_2O_3	Fixed bed	250	40	1/10	2	6	74	67.5	50	0.01	[13]
MoNiAl	Fixed bed	235	45	1/10	12	4	77	33	25.8	1.12	Present work
Mo/NiAl	Fixed bed	235	45	1/10	12	4	69	39	27.0	1.23	Present work

†Estimated values are calculated from data provided in the reference. n.d. no data.
* Physical mixture.

Table 5
Different properties of used catalysts.

Catalysts	S_{BET} (m^2/g)	d^0_{Ni} (nm)	Leaching (%)			C deposits ($\mu mol_{CH4}/g_{cat}$)
			Ni	Mo	Al	
NiAl	59.8 (+38%)	13.8 (+7%)	0.03	n.d.	<0.01	5.8
MoNiAl	37.3 (+8%)	11.2 (+10%)	0.20	0.18	<0.01	15.0
Mo/NiAl	53.4 (+77%)	8.3 (+5%)	0.43	0.02	0.02	5.8

ratio of C/Me (accounting only for –C═O type contribution) was low for all catalysts, accounting for 0.071 for the NiAl assay. Doping with Mo has beneficial effects, particularly for the MoNiAl assay, where the C/Me ratio reduced by 37%, suggesting that Mo is useful in reducing deposition of coke.

H_2-TPR-MS of spent catalysts (Fig. 8B) showed three distinct regions according to CH_4 and water release. In the high temperature region (700–900 °C), only a signal from water was detected, indicating that the H_2 uptake (not shown) corresponds to the reduction of Ni^{2+} in the spinel, in agreement with the TPR_{700} results. In the intermediate temperature range (270–650 °C), signals from both water and CH_4 were detected, indicating hydrogenation of carbonaceous deposits [89]. Finally, in the low temperature region (150–260 °C), only a signal from

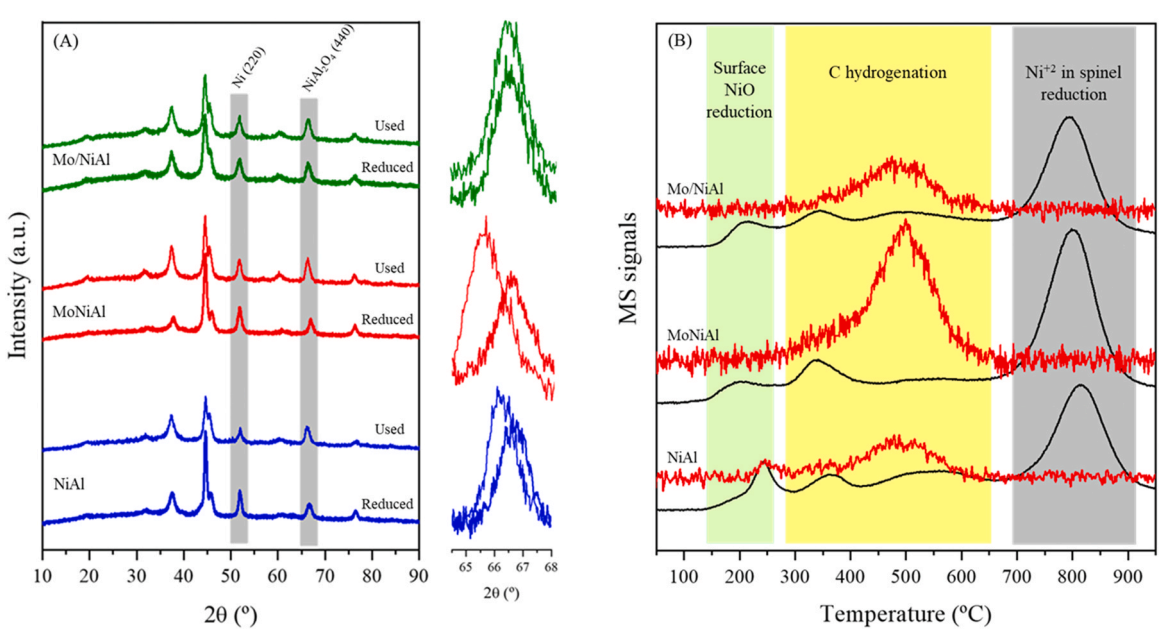

Fig. 8. (A) XRD spectra (with magnification of spinel (440) peak) and (B) H_2-TPR-MS of the spent catalysts. MS signals of water (black lines) and methane (red lines) are normalized by the mass of catalyst. The signal for CH_4 has been magnified 100 times.

water was detected, which could be attributed to the reduction of surface Ni^{2+} as entities such as NiO or its hydrated form $Ni(OH)_2$, confirming some oxidation of the outermost layers of the Ni particles. After calibration of the MS, the area below CH_4 was used to quantify the released CH_4 formed by C hydrogenation. The results showed that the MoNiAl assay had the highest carbonaceous depositions, with three times greater than the other catalysts (Table 5). As anticipated, the reaction in the aqueous phase generates considerably lower carbon deposits in comparison to the vapor phase hydrogenolysis, amounting to a difference of three orders of magnitude [90].

The deposition of carbon was also confirmed by Raman spectroscopy (Fig. S12, ESI), which was used to characterize its structure. In all cases, two characteristic peaks can be observed at around 1340 and 1595 cm^{-1}, attributed to the disordered carbon species (D-band) and graphitic carbon with a high degree of crystallinity (G-band), respectively [91]. The obtained I_D/I_G intensity ratios were in the range of 0.78–1.1, indicating a low degree of graphitization, in agreement with XRD.

Due to the low content of carbonaceous deposits, the deactivation of the catalysts was mainly attributed to the irreversible leaching and oxidation of metals, although these factors are hardly noticeable within 4 h of reaction. Strategies such as coating with carbon, promoting metal-support interaction, and embedding metal particles can prevent metal leaching [92] while reduction treatment is suitable for reducing oxidized metal surfaces and selectively removing carbonaceous deposits [93].

4. Conclusion

Nickel-based catalysts were prepared from stoichiometric nickel aluminate spinel, which was doped with 1 wt% Mo using sol-gel or impregnation methods. The physico-chemical properties of the catalysts were thoroughly characterized alongside their ability to the hydrogenolysis of glycerol with in situ produced H_2. The addition of Mo hindered the reducibility of nickel, but the smaller size of Ni metallic crystallites in the doped assays resulted in a doubling of the density of metal sites, in contrast with NiAl. Furthermore, the introduction of Mo doubled the density of acidic sites. HRTEM uncovered the formation of MoOx entities around the metallic Ni while XPS confirmed the strong Ni-Mo interaction. After doping with Mo, the yield of liquid products deeply increased with the peak yield noted for 1,2-PG. Mo-doping had an impact on product distribution, as evidenced by the increase in the ratio of cleavage products of C-O to C-C. The STY_{PG} (min^{-1}) varied as follows: Mo/NiAl (1.23) ≈ MoNiAl (1.12) > NiAl (0.74), indicating that Mo-doping led to a more efficient arrangement of metal/acid sites, specifically in the Mo/NiAl catalyst. The results revealed that using Mo/NiAl catalyst, at 235 ℃ and 45 bar and 12 h^{-1}, achieved 69% glycerol conversion and also produced the highest yield and selectivity of 1,2-PG at 27% and 39%, respectively. Irreversible leaching and surface oxidation of metals could potentially cause catalyst deactivation, although no such effects were observed during the 4 h reaction period. In conclusion, 1 wt% Mo-doped nickel aluminate-derived catalysts possess potential for the selective production of 1,2-PDO in a eco-friendly process through one-pot coupling H_2 generation via APR and hydrogenolysis reactions.

CRediT authorship contribution statement

Gallego-García Daniel: Investigation, Writing – original draft. **Iriarte-Velasco U.:** Formal analysis, Writing – review & editing. **Gutiérrez-Ortiz M.A.:** Funding acquisition, Resources, Supervision. **Ayastuy Jose Luis:** Conceptualization, Funding acquisition, Supervision, Writing – review & editing.

Declaration of Competing Interest

The authors declare that they have no known competing financial interests or personal relationships that could have appeared to influence the work reported in this paper.

Data availability

Data will be made available on request.

Acknowledgements

This research was supported by grant PID2019-106692RB-I00 funded by MCIN/AEI/10.13039/501100011033. The authors thank for technical support provided by SGIker of UPV/EHU and European funding (ERDF and ESF). DGG would like to thank MICINN for the predoctoral grant (PRE2020-094391).

Appendix A. Supporting information

Supplementary data associated with this article can be found in the online version at doi:10.1016/j.apcatb.2023.123671.

References

[1] W. Wang, L.W. Fan, P. Zhou, Evolution of global fossil fuel trade dependencies, Energy 238 (2022) 121924, https://doi.org/10.1016/j.energy.2021.121924.
[2] M.S. Ardi, M.K. Aroua, N.A. Hashim, Progress, prospect and challenges in glycerol purification process: a review, Renew. Sustain. Energy Rev. 42 (2015) 1164–1173, https://doi.org/10.1016/j.rser.2014.10.091.
[3] R. Mane, Y. Jeon, C. Rode, A review on non-noble metal catalysts for glycerol hydrodeoxygenation to 1,2-propanediol with and without external hydrogen, Green Chem. 24 (2022) 6751–6781, https://doi.org/10.1039/D2GC01879A.
[4] A.V.-H. Soares, G. Perez, F.B. Passos, Alumina supported bimetallic Pt-Fe catalysts applied to glycerol hydrogenolysis and aqueous phase reforming, Appl. Catal. B 185 (2016) 77–87, https://doi.org/10.1016/j.apcatb.2015.11.003.
[5] D.Martin Alonso, S.G. Wettstein, J.A. Dumesic, Bimetallic catalysts for upgrading of biomass to fuels and chemicals, Chem. Soc. Rev. 41 (2012) 8075–8098, https://doi.org/10.1039/C2CS35188A.
[6] L. Petrus, M.A. Noordermeer, Biomass to biofuels, a chemical perspective, Green Chem. 8 (2006) 861–867, https://doi.org/10.1039/B605036K.
[7] S. Chanklang, W. Mondach, P. Somchuea, T. Witoon, M. Chareonpanich, K. Faungnawakij, A. Seubsai, Hydrogenolysis of glycerol to 1,3-propanediol over H-ZSM-5-supported iridium and rhenium oxide catalysts, Catal. Today 397-399 (2022) 356–364, https://doi.org/10.1016/j.cattod.2021.08.014.
[8] B.S. Shrirame, A.R. Varma, S.S. Sahoo, K. Gayen, S.K. Maity, Techno-commercial viability of glycerol valorization to 1,2- and 1,3-propanediol using pinch technology, Biomass Bioenergy 177 (2023) 106943, https://doi.org/10.1016/j.biombioe.2023.106943.
[9] F. Cai, D. Pan, J.J. Ibrahim, J. Zhang, G. Xiao, Hydrogenolysis of glycerol over supported bimetallic Ni/Cu catalysts with and without external hydrogen addition in a fixed-bed flow reactor, Appl. Catal. A Gen. 564 (2018) 172–182, https://doi.org/10.1016/j.apcata.2018.07.029.
[10] X. Jin, B. Yin, Q. Xia, T. Fang, J. Shen, L. Kuang, C. Yang, Catalytic transfer hydrogenation of biomass-derived substrates to value-added chemicals on dual-function catalysts: opportunities and challenges, ChemSusChem 12 (2018) 71–92, https://doi.org/10.1002/cssc.201801620.
[11] J.N. Chheda, G.W. Huber, J.A. Dumesic, Liquid-phase catalytic processing of biomass-derived oxygenated hydrocarbons to fuels and chemicals, Angew. Chem. Int. Ed. 48 (2007) 7164–7183, https://doi.org/10.1002/anie.200604274.
[12] R.M. Ripken, J. Meuldijk, J.G.E. Gardeniers, S. Le Gac, Influence of the water phase state on the thermodynamics of aqueous-phase reforming for hydrogen production, ChemSusChem 10 (2017) 4909–4913, https://doi.org/10.1002/cssc.201700189.
[13] V.G.S. Mendoça, I.C. Freitas, R.L. Manfro, M.M.V.M. Souza, Effect of MgO addition to Cu-Ni/Al_2O_3 catalysts on glycerol hydrogenolysis in continuous reactor without external hydrogen, Appl Catal A Gen. 645 (2022) 118838, https://doi.org/10.1016/j.apcata.2022.118838.
[14] A. Fasolini, D. Cespi, T. Tabanelli, R. Cucciniello, F. Cavani, Hydrogen from renewables: a case study of glycerol reforming, Catalysts 9 (2019) 722, https://doi.org/10.3390/catal9090722.
[15] D.K. Pandey, P. Biswas, Review of the development of heterogeneous catalysts for liquid and vapor phase hydrogenolysis of glycerol to propylene glycol (1,2-propanediol): state-of-the-art and outlook, Energy Fuels 37 (2023) 6879–6906, https://doi.org/10.1021/acs.energyfuels.2c03806.
[16] Y. Nakagawa, M. Tamura, K. Tomishige, Perspective on catalyst development for glycerol Reduction to C3 chemicals with molecular hydrogen, Res. Chem. Intermed. 44 (2018) 3879–3909, https://doi.org/10.1007/s11164-018-3481-2.
[17] S. Dutta, B. Saha, Hydrodeoxygenation of furylmethane oxygenates to jet and diesel range fuels: probing the reaction network with supported palladium catalyst and hafnium triflate promoter, ACS Catal. 7 (2017) 5491–5499, https://doi.org/10.1021/acscatal.7b00986.

[18] M. Checa, V. Montes, J. Hidalgo-Carrillo, A. Marinas, F.J. Urbano, Influence of boron, tungsten and molybdenum modifiers on zirconia based Pt catalyst for glycerol valorization, Nanomaterials 9 (4) (2019) 509, https://doi.org/10.3390/nano9040509.

[19] M.H.M. Pires, F.B. Passos, Y. Xing, Hydrogenolysis of glycerol over ZSM-5 supported ruthenium and copper catalysts: structural study and effects in reaction, Catal. Today 419 (2023) 114161, https://doi.org/10.1016/j.cattod.2023.114161.

[20] E.S. Vasiliadou, E. Heracleous, I.A. Vasalos, A.A. Lemonidou, Ru-based catalysts for glycerol hydrogenolysis-Effect of support and metal precursor, Appl. Catal. B 92 (2009) 90–99, https://doi.org/10.1016/j.apcatb.2009.07.018.

[21] V.S. Marakatti, D. Mumbaraddi, G.V. Shanbhag, A.B. Halgeri, S.P. Maradur, Molybdenum oxide/γ-alumina: an efficient solid acid catalyst for the synthesis of nopol by Prins reaction, RSC Adv. 5 (2015) 93452–93462, https://doi.org/10.1039/C5RA12106J.

[22] P.J. Dietrich, F.G. Sollberger, M.C. Akatay, E.A. Stach, W.N. Delgass, J.T. Miller, F. H. Ribeiro, Structural and catalytic differences in the effect of Co and Mo as promoters for Pt-based aqueous phase reforming catalysis, Appl. Catal. B 156-157 (2014) 236–248, https://doi.org/10.1016/j.apcatb.2014.03.016.

[23] A. Morales-Marín, J.L. Ayastuy, U. Iriarte-Velasco, M.A. Gutiérrez-Ortíz, Nickel aluminate spinel-derived catalysts for the aqueous phase reforming of glycerol: effect of reduction temperature, Appl. Catal. B 244 (2019) 931–945, https://doi.org/10.1016/j.apcatb.2018.12.020.

[24] D. Roy, B. Subramaniam, R.V. Chaudhari, Aqueous phase hydrogenolysis of glycerol to 1,2-propanediol without external hydrogen addition, Catal. Today 156 (2010) 31–37, https://doi.org/10.1016/j.cattod.2010.01.007.

[25] R.B. Mane, C.V. Rode, Simultaneous glycerol dehydration and in situ hydrogenolysis over Cu-Al oxide under an inert atmosphere, Green Chem. 14 (2012) 2780–2789, https://doi.org/10.1039/C2GC35661A.

[26] I.C. Freitas, R.L. Manfro, M.M.V.M. Souza, Hydrogenolysis of glycerol to propylene glycol in continuous system without hydrogen addition over Cu-Ni catalysts, Appl. Catal. B 220 (2018) 31–41, https://doi.org/10.1016/j.apcatb.2017.08.030.

[27] R. Raso, L. García, J. Ruiz, M. Oliva, J. Arauzo, Aqueous phase hydrogenolysis of glycerol over Ni/Al-Fe catalysts without external hydrogen addition, Appl. Catal. B 283 (2021) 119598, https://doi.org/10.1016/j.apcatb.2020.119598.

[28] M. Thommes, K. Kaneko, A.V. Neimark, J.P. Olivier, F. Rodriguez-Reinoso, J. Rouquerol, K.S.W. Sing, Physisorption of gases, with special reference to the evaluation of surface area and pore size distribution (IUPAC Technical Report), Pure Appl. Chem. 87 (2015) 1051–1069, https://doi.org/10.1515/pac-2014-1117.

[29] M.C. Yang, B. Xu, J.H. Cheng, C.J. Pan, B.J. Hwang, Y.S. Meng, Electronic, structural, and electrochemical properties of $LiNi_xCu_yMn_{2-x-y}O_4$ (0< x< 0.5, 0 <y< 0.5) high-voltage spinel materials, Chem. Mater. 23 (2011) 2832–2841, https://doi.org/10.1021/cm200042z.

[30] M.A. Laguna-Bercero, M.L. Sanjuán, R.I. Merino, Raman spectroscopic study of cation disorder in poly- and single crystals of the nickel aluminate spinel, J. Phys. Condens. Matter 19 (2007) 186217, https://doi.org/10.1088/0953-8984/19/18/186217.

[31] Z. Chen, R.G. Kukushkin, P.M. Yeletsky, A.A. Saraev, O.A. Bulavchenko, M. Millan, Coupling hydrogenation of guaiacol with in situ hydrogen production by glycerol aqueous reforming over Ni/Al2O3 and Ni-X/Al2O3 (X = Cu, Mo, P) catalysts, Nanomaterials 10 (2020) 1420, https://doi.org/10.3390/nano10071420.

[32] F. Yang, N.J. Libretto, M.R. Komarneni, W. Zhou, J.T. Miller, X. Zhu, D.E. Resasco, Enhancement of m-cresol hydrodeoxynation selectivity on Ni catalysts by surface decoration of MoO_x species, ACS Catal. 9 (2019) 7791–7800, https://doi.org/10.1021/acscatal.9b01285.

[33] D. Wang, X. Kang, Y. Gu, H. Zhang, J. Liu, A. Wu, H. Yan, C. Tian, H. Fu, Electronic tuning of Ni by Mo species for highly efficient hydroisomerization of n-alkanes comparable to Pt-based catalysts, ACS Catal. 10 (2020) 10449–10458, https://doi.org/10.1021/acscatal.0c01159.

[34] B. Behnejad, M. Abdouss, A. Tavasoli, Comparison of performance of Ni-Mo/γ-alumina catalyst in HDS and HDN reactions of main distillate fractions, Pet. Sci. 16 (2019) 645–656, https://doi.org/10.1007/s12182-019-0319-5.

[35] L. Zhou, L. Li, N. Wei, J. Li, J.M. Basset, Effect of $NiAl_2O_4$ formation on Ni/Al_2O_3 Stability during dry reforming of methane, ChemCatChem 7 (2015) 2508–2516, https://doi.org/10.1002/cctc.201500379.

[36] E. Kordouli, B. Pawelec, C. Kordulis, A. Lycourghiotis, J.L.G. Fierro, Hydrodeoxygenation of phenol on bifunctional Ni-based catalysts: effects of Mo promotion and support, Appl. Catal. B 238 (2018) 147–160, https://doi.org/10.1016/j.apcatb.2018.07.012.

[37] T. Borowiecki, W. Gac, A. Denis, Effects of small MoO_3 additions on the properties of nickel catalysts for the steam reforming of hydrocarbons, Appl. Catal. A Gen. 153 (1997) 141–156, https://doi.org/10.1016/S0926-860X(96)00355-9.

[38] Y. Ma, J. Liu, M. Chu, J. Yue, Y. Cui, G. Xu, Cooperation between active metal and basic support in ni-based catalyst for low-temperature CO_2 methanation, Catal. Lett. 150 (2020) 1418–1426, https://doi.org/10.1007/s10562-019-03033-w.

[39] S. Velu, S.K. Gangwal, Synthesis of alumina supported nickel nanoparticle catalysts and evaluation of nickel metal dispersions by temperature programmed desorption, Solid State Ion. 177 (2006) 803–811, https://doi.org/10.1016/j.ssi.2006.01.031.

[40] Q. Liu, F. Gu, Z. Zhong, G. Xu, F. Su, V-promoted Ni/Al2O3 catalyst for synthetic natural gas (SNG) production: catalyst preparation methodologies, Korean J. Chem. Eng. 33 (2016) 1599–1605, https://doi.org/10.1007/s11814-015-0270-0.

[41] S. Chen, C. Miao, Y. Luo, G. Zhou, K. Xiong, Z. Jiao, X. Zhang, Study of catalytic hydrodeoxygenation performance of Ni catalysts: effects of prepared method, Renew. Energy 115 (2018) 1109–1117, https://doi.org/10.1016/j.renene.2017.09.028.

[42] J. Zhang, L. Chen, Y. Fan, C. Zhao, W. Dai, L. Yang, L. Zhou, J. Zou, X. Luo, Unraveling the high catalytic activity of single atom Mo-doped TiO_2 towards NH_3-SCR: synergetic roles of Mo as acid sites and oxygen vacancies as oxidation sites, Chem. Eng. J. 465 (2023) 142759, https://doi.org/10.1016/j.cej.2023.142759.

[43] W. Tan, J. Wang, Y. Cai, L. Li, S. Xie, F. Gao, F. Liu, L. Dong, Molybdenum oxide as an efficient promoter to enhance the NH_3-SCR performance of CeO_2-SiO_2 catalyst for NO_x removal, Catal. Today 397-399 (2022) 475–483, https://doi.org/10.1016/j.cattod.2021.07.007.

[44] T. Kitano, S. Okazaki, T. Shishido, K. Teramura, T. Tanaka, Brønsted acid generation of alumina-supported molybdenum oxide calcined at high temperatures: Characterization by acid-catalyzed reactions and spectroscopic methods, J. Mol. Catal. A Chem. 371 (2013) 21–28, https://doi.org/10.1016/j.molcata.2013.01.019.

[45] S. Sreekantan, A.A.B. Kirali, B. Marimuthu, Catalytic conversion of sucrose to 1,2-propanediol over alumina-supported Ni-Mo bimetallic catalysts, Sustain. Energy Fuels 6 (2022) 3681–3689, https://doi.org/10.1039/D2SE00610C.

[46] J. Harmel, L.I. Van der Wal, J. Zečević, P.E. de Jongh, K.P. de Jong, Influence of intimacy for metal-mesoporous solid acids catalysts for *n*-alkanes hydroconversion, Catal. Sci. Technol. 10 (2020) 2111–2119, https://doi.org/10.1039/C9CY02510C.

[47] J.P. Thielemann, T. Ressler, A. Walter, G. Tzolova-Müller, C. Hess, Strcture of molybdenum oxide supported on silica SBA-15 studied by Raman, UV-Vis and X-ray absorption spectroscopy, Appl. Catal. A Gen. 399 (2011) 28–34, https://doi.org/10.1016/j.apcata.2011.03.032.

[48] S. Zhang, M. Ying, J. Yu, W. Zhan, L. Wang, Y. Guo, Y. Guo, $Ni_xA_lO_2$-δ mesoporous catalysts for dry reforming of methane: the special role of NiAl2O4 spinel phase and its reaction mechanism, Appl. Catal. B 291 (2021) 120074, https://doi.org/10.1016/j.apcatb.2021.120074.

[49] H. Tian, C.A. Roberts, I.E. Wachs, Molecular structural determination of Molybdena in different environments: aqueous solutions, bulk mixed oxides, and supported MoO_3 catalysts, J. Phys. Chem. C 114 (2010) 14110–14120, https://doi.org/10.1021/jp103269w.

[50] Q. Bkour, F. Che, K.M. Lee, C. Zhou, N. Akter, J.A. Boscoboinik, K. Zhao, J.T. Gray, S.R. Saunders, M.G. Norton, J.S. McEwen, T. Kim, S. Ha, Enhancing the partial oxidation of gasolina with Mo-doped Ni catalysts for SOFC applications: an integrated experimental and DFT study, Appl. Catal. B 266 (2020) 118626, https://doi.org/10.1016/j.apcatb.2020.118626.

[51] T.L. Drake, P.C. Stair, Multiwavelength Raman spectroscopic characterization of alumina-supported molybdenum oxide prepared by vapor deposition, Top. Catal. 60 (2017) 1618–1630, https://doi.org/10.1007/s11244-017-0842-9.

[52] L. Zhang, X. Wang, X. Shang, M. Tan, W. Ding, X. Lu, Carbon dioxide reforming of methane over mesoporous nickel aluminate/γ-alumina composites, J. Energy Chem. 26 (2017) 93–100, https://doi.org/10.1016/j.jechem.2016.08.001.

[53] A.J. Pamphile-Adrian, F.B. Passos, P.P. Florez-Rodriguez, Systematic study on the properties of nickel aluminate ($NiAl_2O_4$) as a catalytic precursor for aqueous phase hydrogenolysis of glycerol, Catal. Today 394-396 (2022) 499–509, https://doi.org/10.1016/j.cattod.2021.07.002.

[54] C. Ranga, R. Lødeng, V.I. Alexiadis, T. Rajkhowa, H. Bjørkan, S. Chytil, I. H. Svenum, J. Walmsley, C. Detavernier, H. Poelman, P. Van der Voort, J. W. Thybaut, Effect of composition and preparation of supported MoO_3 catalysts for anisole hydrodeoxygenation, Chem. Eng. J. 335 (2018) 120–132, https://doi.org/10.1016/j.cej.2017.10.090.

[55] M.H. Aghaali, S. Firoozi, Enhancing the catalytic performance of Co substituted $NiAl_2O_4$ spinel by ultrasonic spray pyrolysis method for steam and dry reforming of methane, Int. J. Hydrog. Energy 46 (2021) 357–373, https://doi.org/10.1016/j.ijhydene.2020.09.157.

[56] A. Velon, I. Olefjord, Oxidation behavior of Ni3Al and Fe3Al: II. Early stage of oxide growth, Oxid. Met. 56 (2001) 425–452, https://doi.org/10.1023/A:1012537331730.

[57] J.G. Baker, J.R. Schneider, J.A. Garrido Torres, J.A. Singh, A.J.M. Mackus, M. Bajdich, S.F. Bent, The role of aluminum in promoting Ni-Fe-OOH electrocatalysts for the oxygen evolution reaction, ACS Appl. Energy Mater. 2 (2019) 3488–3499, https://doi.org/10.1021/acsaem.9b00265.

[58] M.S. Yancheshmeh, O.A. Sahraei, M. Aissaoui, M.C. Iliuta, A novel synthesis of $NiAl_2O_4$ spinel from a Ni-Al mixed-metal alkoxide as a highly efficient catalyst for hydrogen production by glycerol steam reforming, Appl. Catal. B 265 (2020) 118535, https://doi.org/10.1016/j.apcatb.2019.118535.

[59] T. Sun, G. Wang, X. Guo, Z. Li, E. Wang, C. Li, A highly active NiMoAl catalyst prepared by a solvothermal method for the hydrogenation of methyl acrylate, Catalysts 12 (2022) 1118, https://doi.org/10.3390/catal12101118.

[60] S.M. Gericke, J. Rissler, M. Bermeo, H. Wallander, H. Karlsson, L. Kollberg, M. Scardamaglia, R. Temperton, S. Zhu, K.G.V.S. Clauss, C. Hulteberg, A. Shavorskiy, L.R. Merte, M.E. Messing, J. Zetterberg, S. Bolmberg, In situ H_2 reduction of Al_2O_3-supported Ni- and Mo-based catalysts, Catalysts 12 (2022) 755, https://doi.org/10.3390/catal12070755.

[61] C. Yang, W. Wang, D. Wang, M. Gong, Y. Xin, L. Xiao, O.V. Kikhtyanin, D. Kubicka, W. Wu, The promotion effects of MoOx species in the highly effective NiMo/$MgAl_2O_4$ catalysts for the hydrodeoxygenation of methyl palmitate, J. Environ. Chem. Eng. 10 (2022) 107761, https://doi.org/10.1016/j.jece.2022.107761.

[62] M.L. Ang, U. Oemar, E.T. Saw, L. Mo, Y. Kathiraser, B.H. Chia, S. Kawi, Highly active Ni/xNa/CeO_2 catalyst for the water–gas shift reaction: effect of sodium on methane suppression, ACS Catal. 4 (2014) 3237–3248, https://doi.org/10.1021/cs500915p.

[63] J. Gao, Q. Liu, F. Gu, B. Liu, Z. Zhong, F. Su, Recent advances in methanation catalysts for the production of synthetic natural gas, RSC Adv. 5 (2015) 22579–22776, https://doi.org/10.1039/C4RA16114A.

[64] G.K. Reddy, P. Boolchand, P.G. Smirniotis, Sulfur tolerant metal doped Fe/Ce catalysts for high temperature WGS reaction at low steam to CO ratios – XPS and Mössbauer spectroscopic study, J. Catal. 282 (2011) 258–269, https://doi.org/10.1016/j.jcat.2011.06.016.
[65] K. Tomishige, Y. Nakagawa, M. Tamura, Selective hydrogenolysis and hydrogenation using metal catalysts directly modified with metal oxide species, Green Chem. 19 (2017) 2876–2924, https://doi.org/10.1039/C7GC00620A.
[66] A.D. da Silva Ruy, R.M. de Brito Alves, T.L. Reis Hewer, D. de Aguilar Pontes, L. S. Gomes Teixeira, L.A. Magalhães Pontes, Catalysts for glycerol hydrogenolysis to 1,3-propanediol: a review of chemical routes and market, Catal. Today 381 (2021) 243–253, https://doi.org/10.1016/j.cattod.2020.06.035.
[67] M.R. Md Radzi, M.D. Manogaran, M.H.M. Yusoff, Zulqarnain, M.R. Anuar, N. F. Shoparwe, M.F. Ab Rahman, Production of propanediols through in situ glycerol hydrogenolysis via aqueous phase reforming: a review, Catalysts 12 (2022) 945, https://doi.org/10.3390/catal12090945.
[68] J. Wang, X. Zhao, N. Lei, L. Li, L. Zhang, S. Xu, S. Miao, X. Pan, A. Wang, T. Zhang, Hydrogenolysis of glycerol to 1,3-propanediol under low hydrogen pressure over WOx-supported single/Pseudo-single atom Pt catalyst, ChemSusChem 9 (2016) 794–800, https://doi.org/10.1002/cssc.201501506.
[69] M.L. Shozi, V.D.B.C. Dasireddy, S. Singh, P. Mohlala, D.J. Morgan, H.B. Friedrich, Hydrogenolysis of glycerol to monoalcohols over supported Mo and W catalysts, ACS Sustain. Chem. Eng. 4 (2016) 5752–5760, https://doi.org/10.1021/acssuschemeng.6b01675.
[70] D. Mei, A.M. Karim, Y. Wang, Density functional theory study of acetaldehyde hydrodeoxygenation on MoO_3, J. Phys. Chem. C 115 (2011) 8155–8164, https://doi.org/10.1021/jp200011j.
[71] K. Tomishige, Y. Nakagawa, M. Tamura, Selective hydrogenolysis of C-O bonds using the interaction of the catalyst surface and OH groups, Top. Curr. Chem. 353 (2014) 127–162, https://doi.org/10.1007/128_2014_538.
[72] F. Cai, X. Song, Y. Wu, J. Zhang, G. Xiao, Selective hydrogenolysis of glycerol over acid-modified Co–Al catalysts in a fixed-bed flow reactor, ACS Sustain. Chem. Eng. 6 (2018) 110–118, https://doi.org/10.1021/acssuschemeng.7b01233.
[73] I. Coronado, M. Stekrova, M. Reinikainen, P. Simell, L. Lefferts, J. Lehtonen, A review of catalytic aqueous-phase reforming of oxygenated hydrocarbons derived from biorefinery water fractions, Int. J. Hydrog. Energy 41 (2016) 11003–11032, https://doi.org/10.1016/j.ijhydene.2016.05.032.
[74] L. García, A. Valiente, M. Oliva, J. Ruiz, J. Arauzo, Influence of operating variables on the aqueous-phase reforming of glycerol over a Ni/Al coprecipitated catalyst, Int. J. Hydrog. Energy 43 (2018) 20392–20407, https://doi.org/10.1016/j.ijhydene.2018.09.119.
[75] A. Seretis, P. Tsiakaras, Hydrogenolysis of glycerol to propylene glycol by in situ produced hydrogen from aqueous phase reforming of glycerol over SiO_2-Al_2O_3 supported nickel catalyst, Fuel Process. Technol. 142 (2016) 135–146, https://doi.org/10.1016/j.fuproc.2015.10.013.
[76] C.H. Zhou, K. Deng, M.D. Serio, S. Xiao, D.S. Tong, L. Li, C.X. Lin, J. Beltramini, H. Zhang, W.H. Yu, Cleaner hydrothermal hydrogenolysis of glycerol to 1,2-propanediol over Cu/oxide catalysts without addition of external hydrogen, Mol. Catal. 432 (2017) 274–284, https://doi.org/10.1016/j.mcat.2017.02.008.
[77] A. Syuhada, M. Ameen, M.T. Azizan, A. Aqsha, M.H.M. Yusoff, A. Ramli, M. S. Alnarabiji, F. Sher, In-situ hydrogenolysis of glycerol using hydrogen produced via aqueous phase reforming of glycerol over sonochemically synthesized nickel-based nano-catalyst, Mol. Catal. 514 (2021) 111860, https://doi.org/10.1016/j.mcat.2021.111860.
[78] X. Jin, B. Subramaniam, R.V. Chaudhari, P.S. Thapa, Kinetic modeling of Pt/C catalyzed aqueous phase glycerol conversion with in situ formed hydrogen, AIChE J. 62 (2016) 1162–1173, https://doi.org/10.1002/aic.15114.
[79] M.L. Barbelli, G.F. Santori, N.N. Nichio, Aqueous phase hydrogenolysis of glycerol to bio-propylene glycol over Pt-Sn catalysts, Bioresour. Technol. 111 (2012) 500–503, https://doi.org/10.1016/j.biortech.2012.02.053.
[80] T. van Haasterecht, C.C.I. Ludding, K.P. de Jong, J.H. Bitter, Stability and activity of carbon nanofiber-supported catalysts in the aqueous phase reforming of ethylene glycol, J. Energy Chem. 22 (2013) 257–269, https://doi.org/10.1016/S2095-4956(13)60032-7.
[81] I. Sádaba, M. López Granados, A. Riisager, E. Taarning, Deactivation of solid catalysts in Liquid media: the case of leaching of active sites in biomass conversion reactions, Green Chem. 17 (2015) 4133–4145, https://doi.org/10.1039/C5GC00804B.
[82] R.M. Ravenelle, J.R. Copeland, W.G. Kim, J.C. Crittenden, C. Sievers, Structural changes of γ-Al_2O_3-supported catalysts in hot liquid water, ACS Catal. 1 (2011) 552–561, https://doi.org/10.1021/cs1001515.
[83] T. van Haasterecht, M. Swart, K.P. de Jong, J.H. Bitter, Effect of initial nickel particle size on stability of nickel catalysts for aqueous phase reforming, J. Energy Chem. 25 (2016) 289–296, https://doi.org/10.1016/j.jechem.2016.01.006.
[84] N.M. Eagan, J.P. Chada, A.M. Wittrig, J.S. Buchanan, J.A. Dumesic, G.W. Huber, Hydrodeoxygenation of sorbitol to monofunctional fuel precursors over Co/TiO_2, Joule 1 (2017) 178–199, https://doi.org/10.1016/j.joule.2017.07.004.
[85] D.S. Hall, D.J. Lockwood, C. Bock, B.R. MacDougall, Nickel hydroxides and related materials: a review of their structures, synthesis and properties, Proc. R. Soc. A 471 (2015) 0792, https://doi.org/10.1098/rspa.2014.0792.
[86] L.E. Strange, V. Shutthanandan, M. Song, M. Bowden, Q.R.S. Miller, R. Prabhakaran, R. Shimskey, V.V. Joshi, Multimodal analysis and characterization of the boehmite layer formed on AA6061 before and after alkaline etching, J. Mater. Res. Technol. 21 (2022) 1274–1281, https://doi.org/10.1016/j.jmrt.2022.09.125.
[87] M. El Doukkali, S. Paul, F. Dumeignil, New insights in single-step hydrodeoxygenation of glycerol to propylene by coupling rational catalyst design with systematic analysis, Appl. Catal. B 324 (2023) 122280, https://doi.org/10.1016/j.apcatb.2022.122280.
[88] A.J. Reynoso, J.L. Ayastuy, U. Iriarte-Velasco, M.A. Gutiérrez-Ortíz, Bio-hydrogen and valuable chemicals from industrial waste glycerol via catalytic aqueous-phase transformation, Fuel Process. Technol. 242 (2023) 107634, https://doi.org/10.1016/j.fuproc.2022.107634.
[89] A.J. Reynoso, U. Iriarte-Velasco, M.A. Gutiérrez-Ortíz, J.L. Ayastuy, Highly stable Pt/$CoAl_2O_4$ catalysts in Aqueous-Phase Reforming of glycerol, Catal. Today 367 (2021) 278–289, https://doi.org/10.1016/j.cattod.2020.03.039.
[90] S. Zhu, X. Gao, Y. Zhu, W. Fan, J. Wang, Y. Li, A highly efficient and robust Cu/SiO_2 catalyst prepared by the ammonia evaporation hydrothermal method for glycerol hydrogenolysis to 1,2-propanediol, Catal. Sci. Technol. 5 (2015) 1169–1180, https://doi.org/10.1039/C4CY01148A.
[91] K.N. Papageridis, G. Siakavelas, N.D. Charisiou, D.G. Avraam, L. Tzounis, K. Kousi, M.A. Goula, Comparative study of Ni, Co, Cu supported on γ-alumina catalysts for hydrogen production via the glycerol steam reforming reaction, Fuel Process. Technol. 152 (2016) 156–175, https://doi.org/10.1016/j.fuproc.2016.06.024.
[92] J. Huo, J.P. Tessonnier, B.H. Shanks, Improving hydrothermal stability of supported metal catalysts for biomass conversions: a review, ACS Catal. 11 (2021) 5248–5270, https://doi.org/10.1021/acscatal.1c00197.
[93] D. Durán-Martín, M. Ojeda, M.L.ópez Granados, J.L.G. Fierro, R. Mariscal, Stability and regeneration of Cu-ZrO_2 catalysts used in glycerol hydrogenolysis to 1,2-propanediol, Catal. Today 210 (2013) 98–105, https://doi.org/10.1016/j.cattod.2012.11.013.